

Parton-Hadron-String Dynamics: an off-shell transport approach for relativistic energies

W. Cassing^a and E. L. Bratkovskaya^{b,*}

^a*Institut für Theoretische Physik, Universität Giessen, Heinrich-Buff-Ring 16,
D-35392 Giessen, Germany*

^b*Institut für Theoretische Physik, JWG Universität Frankfurt, D-60438 Frankfurt
am Main, Germany*

Abstract

The dynamics of partons, hadrons and strings in relativistic nucleus-nucleus collisions is analyzed within the novel Parton-Hadron-String Dynamics (PHSD) transport approach, which is based on a dynamical quasiparticle model for partons (DQPM) matched to reproduce recent lattice-QCD results - including the partonic equation of state - in thermodynamic equilibrium. Scalar- and vector-interaction densities are extracted from the DQPM as well as effective scalar- and vector-mean fields for the partons. The transition from partonic to hadronic degrees of freedom is described by covariant transition rates for the fusion of quark-antiquark pairs or three quarks (antiquarks), respectively, obeying flavor current-conservation, color neutrality as well as energy-momentum conservation. Since the dynamical quarks and antiquarks become very massive close to the phase transition, the formed resonant 'pre-hadronic' color-dipole states ($q\bar{q}$ or qqq) are of high invariant mass, too, and sequentially decay to the groundstate meson and baryon octets increasing the total entropy. The PHSD approach is applied to nucleus-nucleus collisions from 20 to 160 A·GeV in order to explore the space-time regions of 'partonic matter'. We find that even central collisions at the top-SPS energy of 158 A·GeV show a large fraction of non-partonic, i.e. hadronic or string-like matter, which can be viewed as a hadronic corona. This finding implies that neither hadronic nor only partonic 'models' can be employed to extract physical conclusions in comparing model results with data. On the other hand - studying in detail Pb+Pb reactions from 40 to 158 A·GeV - we observe that the partonic phase has a very low impact on rapidity distributions of hadrons but a sizeable influence on the transverse mass distribution of final kaons due to the repulsive partonic mean fields. Furthermore, we find a significant effect on the production of multi-strange antibaryons due to a slightly enhanced $s\bar{s}$ pair production in the partonic phase from massive time-like gluon decay and a larger formation of antibaryons in the hadronization process.

Key words: Quark-gluon plasma, General properties of QCD, Relativistic heavy-ion collisions

1 Introduction

The 'Big Bang' scenario implies that in the first micro-seconds of the universe the entire state has emerged from a partonic system of quarks, antiquarks and gluons – a quark-gluon plasma (QGP) – to color neutral hadronic matter consisting of interacting hadronic states (and resonances) in which the partonic degrees of freedom are confined. The nature of confinement and the dynamics of this phase transition has motivated a large community for several decades and is still an outstanding question of today's physics. Early concepts of the QGP were guided by the idea of a weakly interacting system of partons which might be described by perturbative QCD (pQCD). However, experimental observations at the Relativistic Heavy Ion Collider (RHIC) indicated that the new medium created in ultrarelativistic Au+Au collisions is interacting more strongly than hadronic matter (cf. [1] and Refs. therein) and consequently this concept had to be severely questioned. Moreover, in line with theoretical studies in Refs. [2–4] the medium showed phenomena of an almost perfect liquid of partons [5,6] as extracted from the strong radial expansion and the scaling of elliptic flow $v_2(p_T)$ of mesons and baryons with the number of constituent quarks and antiquarks [5].

The question about the properties of this (nonperturbative) QGP liquid is discussed controversially in the literature and dynamical concepts describing the formation of color neutral hadrons from colored partons are scarce [7–13]. A fundamental issue for hadronization models is the conservation of 4-momentum as well as the entropy problem because by fusion/coalescence of massless (or low constituent mass) partons to color neutral bound states of low invariant mass (e.g. pions) the number of degrees of freedom and thus the total entropy is reduced in the hadronization process [9–11]. This problem - a violation of the second law of thermodynamics as well as the conservation of four-momentum and flavor currents - has been addressed in Ref. [14] on the basis of the DQPM employing covariant transition rates for the fusion of 'massive' quarks and antiquarks to color neutral hadronic resonances or strings. In fact, the dynamical studies for an expanding partonic fireball in Ref. [14] suggest that the latter problems have come to a practical solution.

A consistent dynamical approach - valid also for strongly interacting systems - can be formulated on the basis of Kadanoff-Baym (KB) equations [15,16] or off-shell transport equations in phase-space representation, respectively [16–19]. In the KB

* corresponding author

Email address: Elena.Bratkovskaya@th.physik.uni-frankfurt.de (E. L. Bratkovskaya).

theory the field quanta are described in terms of dressed propagators with complex selfenergies. Whereas the real part of the selfenergies can be related to mean-field potentials (of Lorentz scalar, vector or tensor type), the imaginary parts provide information about the lifetime and/or reaction rates of time-like 'particles' [4]. Once the proper (complex) selfenergies of the degrees of freedom are known the time evolution of the system is fully governed by off-shell transport equations (as described in Refs. [16–19]).

The determination/extraction of complex selfenergies for the partonic degrees of freedom has been performed before in Refs. [4,20,21] by fitting lattice QCD (lQCD) 'data' within the Dynamical QuasiParticle Model (DQPM). In fact, the DQPM allows for a simple and transparent interpretation of lattice QCD results for thermodynamic quantities as well as correlators and leads to effective strongly interacting partonic quasiparticles with broad spectral functions. We stress that mean-field potentials for the 'quarks' and 'gluons' as well as effective interactions have been extracted from lQCD within the DQPM as well (cf. Ref. [21]). For a review on off-shell transport theory and results from the DQPM in comparison to lQCD we refer the reader to Ref. [19].

In a preceding work [14] we have presented first Parton-Hadron-String-Dynamics (PHSD) transport calculations for expanding partonic fireballs of ellipsoidal shape in coordinate space that hadronize according to local covariant transitions. It was found that the resulting particle ratios turn out to be in line with those from a grandcanonical partition function at temperature $T \approx 170$ MeV rather independent from the initial temperature. Furthermore, the scaling of elliptic flow with initial spatial eccentricity indicated a dynamical evolution of the system close to ideal hydrodynamics. These general properties of PHSD results for idealized systems is well in line with global observations of experiments at the Relativistic-Heavy-Ion-Collider (RHIC) [5]. However, the actual question is about the description of various experimental observables in relativistic nuclear systems where a rather precise experimental control is possible.

In the present work we will use an update of the DQPM parameters since more precise lQCD calculations for 2+1 flavors with almost physical quark masses have become available in 2008 [22]. Furthermore, we extend the study in Refs. [20,21] by fixing independently scalar- and vector-interaction densities for the fermion degrees of freedom. Accordingly, the paper is organized as follows: In Section 2 we describe the PHSD approach, present an update of the DQPM results in comparison to lQCD [22] and specify the covariant hadronization scheme employed as well as the elastic and inelastic partonic cross sections. Section 3 is devoted to actual applications of Pb +Pb collisions at SPS energies in comparison to recent experimental data from the NA49 Collaboration. Section 4 concludes this study with a summary and discussion of open problems.

2 The PHSD approach

The Parton-Hadron-String-Dynamics (PHSD) approach is a microscopic covariant transport model that incorporates effective partonic as well as hadronic degrees of freedom and involves a dynamical description of the hadronization process from partonic to hadronic matter. Whereas the hadronic part is essentially equivalent to the conventional Hadron-Strings-Dynamics (HSD) approach [25,26] the partonic dynamics is based on the Dynamical QuasiParticle Model (DQPM) [20,21,27] which describes QCD properties in terms of single-particle Green's functions (in the sense of a two-particle irreducible (2PI) approach).

2.1 Reminder of the DQPM

We briefly recall the basic assumptions of the DQPM: Following Ref. [27] the dynamical quasiparticle mass (for gluons and quarks) is assumed to be given by the thermal mass in the asymptotic high-momentum regime, which is proportional to the coupling $g(T/T_c)$ and the temperature T , i.e. for gluons

$$M_g^2(T) = \frac{g^2(T/T_c)}{6} \left((N_c + \frac{1}{2}N_f) T^2 + \frac{N_c}{2} \sum_q \frac{\mu_q^2}{\pi^2} \right), \quad (1)$$

and for quarks (assuming vanishing constituent masses here) as,

$$M_q^2(T) = \frac{N_c^2 - 1}{8N_c} g^2(T/T_c) \left(T^2 + \frac{\mu_q^2}{\pi^2} \right), \quad (2)$$

with a running coupling (squared) (for $T > T_s$),

$$g^2(T/T_c) = \frac{48\pi^2}{(11N_c - 2N_f) \ln(\lambda^2(T/T_c - T_s/T_c)^2)}, \quad (3)$$

which permits for an enhancement near the critical temperature T_c . Here $N_c = 3$ stands for the number of colors while N_f denotes the number of flavors. The parameters controlling the infrared enhancement of the coupling λ and T_s have been refitted compared to Ref. [27] to the recent IQCD results from Ref. [22] (see below).

The width for gluons and quarks (for $\mu_q = 0$) is adopted in the form [28]

$$\gamma_g(T) = N_c \frac{g^2 T}{8\pi} \ln \frac{2c}{g^2}, \quad \gamma_q(T) = \frac{N_c^2 - 1}{2N_c} \frac{g^2 T}{8\pi} \ln \frac{2c}{g^2}. \quad (4)$$

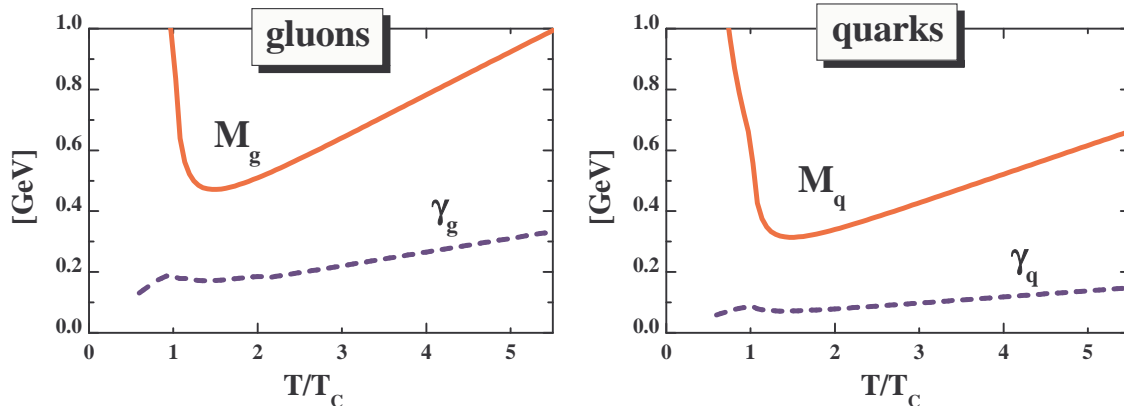


Fig. 1. The effective gluon mass M_g and width γ_g as function of temperature T/T_c (l.h.s.). The r.h.s. shows the corresponding quantities for quarks.

where the parameter c is related to a magnetic cut-off. We stress that a non-vanishing width γ is the central difference of the DQPM to conventional quasiparticle models [29–32]. Its influence is essentially seen in correlation functions as e.g. in the stationary limit of the correlation function in the off-diagonal elements of the energy-momentum tensor T^{kl} which defines the shear viscosity η of the medium [4,33]. Here a sizable width is mandatory to obtain a small ratio in the shear viscosity to entropy density η/s [4].

The actual gluon mass M_g and width γ_g – employed in the further calculations – as well as the quark mass M_q and width γ_q are depicted in Fig. 1 on the lhs and rhs, respectively, as a function of T/T_c . These values for the masses and widths are smaller than those presented in Ref. [27] since the recent lQCD calculations [22] have been performed with much smaller bare fermion masses. This, in fact, leads to an increase in the entropy density $s(T/T_c)$ relative to earlier lQCD calculations, which implies that the quasiparticle mass and width - fitting the lQCD results - become smaller relative to Refs. [20,21,27].

In line with Ref. [27] the parton spectral functions are no longer δ - functions in the invariant mass squared but taken as

$$\rho_j(\omega) = \frac{\gamma_j}{E_j} \left(\frac{1}{(\omega - E_j)^2 + \gamma_j^2} - \frac{1}{(\omega + E_j)^2 + \gamma_j^2} \right) \quad (5)$$

separately for quarks and gluons ($j = q, \bar{q}, g$). With the convention $E^2(\mathbf{p}) = \mathbf{p}^2 + M_j^2 - \gamma_j^2$, the parameters M_j^2 and γ_j are directly related to the real and imaginary parts of the retarded self-energy, e.g. $\Pi_j = M_j^2 - 2i\gamma_j\omega$. The spectral function (5) is antisymmetric in ω and normalized as

$$\int_{-\infty}^{\infty} \frac{d\omega}{2\pi} \omega \rho_j(\omega, \mathbf{p}) = \int_0^{\infty} \frac{d\omega}{2\pi} 2\omega \rho_j(\omega, \mathbf{p}) = 1. \quad (6)$$

With the spectral functions fixed by Eqs. (1)-(5) the total energy density in the DQPM $T_+^{00} + T_-^{00}$ can be evaluated as [21]

$$\begin{aligned}
T_{\pm}^{00} = & d_g \int_0^{\infty} \frac{d\omega}{2\pi} \int \frac{d^3p}{(2\pi)^3} 2\omega^2 \rho_g(\omega, \mathbf{p}) n_B(\omega/T) \Theta(\pm p^2) \\
& + d_q \int_0^{\infty} \frac{d\omega}{2\pi} \int \frac{d^3p}{(2\pi)^3} 2\omega^2 \rho_q(\omega, \mathbf{p}) n_F((\omega - \mu_q)/T) \Theta(\pm p^2) \\
& + d_{\bar{q}} \int_0^{\infty} \frac{d\omega}{2\pi} \int \frac{d^3p}{(2\pi)^3} 2\omega^2 \rho_{\bar{q}}(\omega, \mathbf{p}) n_F((\omega + \mu_q)/T) \Theta(\pm p^2) ,
\end{aligned} \tag{7}$$

where n_B and n_F denote the Bose and Fermi functions, respectively, while μ_q stands for the quark chemical potential. The number of transverse gluonic degrees of freedom is $d_g = 16$ while the fermion degrees of freedom amount to $d_q = d_{\bar{q}} = 2N_c N_f = 18$ in case of three flavors ($N_f=3$). The indices \pm stand for the time-like (+) and space-like part (-) of the energy density (7) as defined via $\Theta(\pm p^2)$ with $p^2 = \omega^2 - \mathbf{p}^2$.

The pressure $P(T)$ then can be obtained by integrating the differential thermodynamic relation (for $\mu_q = 0$)

$$P - T \frac{\partial P}{\partial T} = -T^{00} = P - T s \tag{8}$$

with the entropy density $s(T)$ given by

$$s = \frac{\partial P}{\partial T} = \frac{T^{00} + P}{T} . \tag{9}$$

This approach is thermodynamically consistent and represents a two-particle irreducible (2PI) approximation to hot QCD (once the free parameters in (1) and (2) are fitted to lattice QCD results.)

For the further presentation of the DQPM it is useful to introduce the shorthand notations (following [21])

$$\begin{aligned}
\tilde{\text{T}}r_g^{\pm} \dots &= d_g \int \frac{d\omega}{2\pi} \frac{d^3p}{(2\pi)^3} 2\omega \rho_g(\omega) \Theta(\omega) n_B(\omega/T) \Theta(\pm p^2) \dots \\
\tilde{\text{T}}r_q^{\pm} \dots &= d_q \int \frac{d\omega}{2\pi} \frac{d^3p}{(2\pi)^3} 2\omega \rho_q(\omega) \Theta(\omega) n_F((\omega - \mu_q)/T) \Theta(\pm p^2) \dots \\
\tilde{\text{T}}r_{\bar{q}}^{\pm} \dots &= d_{\bar{q}} \int \frac{d\omega}{2\pi} \frac{d^3p}{(2\pi)^3} 2\omega \rho_{\bar{q}}(\omega) \Theta(\omega) n_F((\omega + \mu_q)/T) \Theta(\pm p^2) \dots
\end{aligned} \tag{10}$$

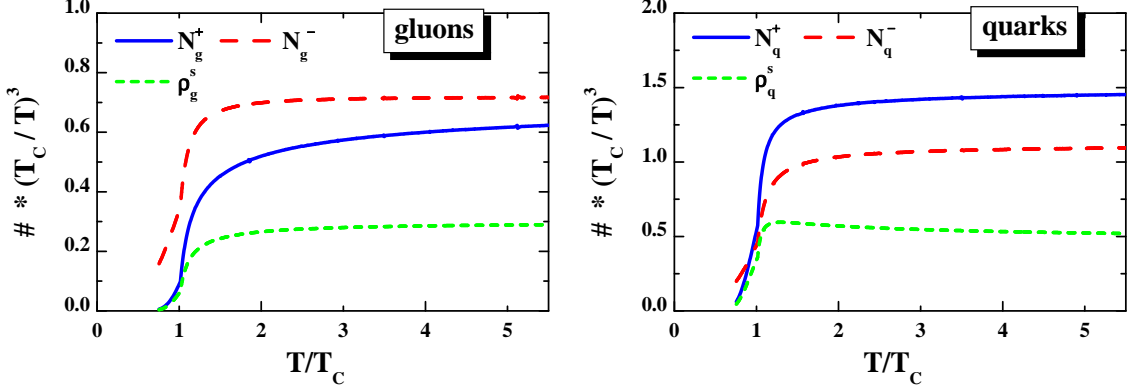


Fig. 2. The time-like (solid line) and space-like (dashed line) gluon 'densities' (10) as well as the scalar gluon density (11) (dotted line) as a function of T/T_c (l.h.s.). The r.h.s. shows the same quantities for quarks + antiquarks. The unit volume considered in these figures is 1 fm^3 . All quantities here have been multiplied by $(T_c/T)^3$ to map out the scaling properties with temperature T .

with $p^2 = \omega^2 - \mathbf{p}^2$ denoting the invariant mass squared. Here the $\Theta(\pm p^2)$ -functions project on 'time-like' (+) and 'space-like' (-) sectors of the four-momentum. The traces in (10) then give directly time-like and space-like 'densities' for gluons N_g^\pm as well as for quarks N_q^\pm (and antiquarks). Note, that only the time-like parts have the physical interpretation of particles per volume.

For the present set of parameters (fitted to the recent IQCD results from Ref. [22] and giving the quasiparticle mass and width as in Fig. 1) the time-like and space-like densities of quarks(+ antiquarks) and gluons are presented in Fig. 2 together with the scalar gluon and quark (+antiquark) densities (lower dotted lines)

$$\rho_g^s(T/T_c) = Tr_g^+ \left(\frac{\sqrt{p^2}}{\omega} \right), \quad \rho_q^s(T/T_c) = Tr_q^+ \left(\frac{\sqrt{p^2}}{\omega} \right) + Tr_{\bar{q}}^+ \left(\frac{\sqrt{p^2}}{\omega} \right). \quad (11)$$

As seen from Fig. 2 the 'densities' roughly scale with $(T/T_c)^3$ except for the region close to T_c . While N_g^+ is lower than N_g^- - implying that more than half of the gluons are 'virtual' - the time-like quark and antiquark densities dominate over the space-like quantities.

The time- and space-like energy densities T_\pm^{00} for gluons and quarks (+ antiquarks) are displayed in Fig. 3 as a function of T/T_c for the present parameter set in units of GeV/fm^3 . Comparable to the case of the 'densities' in Fig. 2 the space-like energy density for gluons is slightly larger than the time-like part whereas the fermion contribution (quarks + antiquarks) is clearly dominated by the time-like sector. All quantities roughly scale as $(T/T_c)^4$ except for the region close to T_c again.

A direct comparison of the entropy density $s(T)$ and energy density $\epsilon(T)$ from the DQPM with results from IQCD from Ref. [22] is presented in Fig. 4. Both results have been divided by T^3 and T^4 , respectively, to demonstrate the scaling with tem-

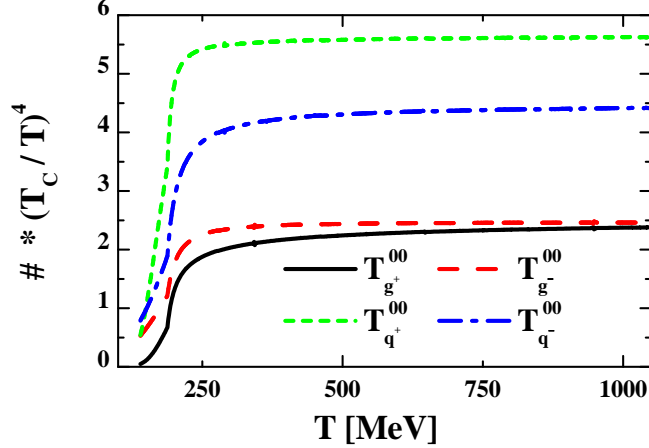


Fig. 3. The different time- and space-like contributions to the total energy density as a function of T/T_c in units of GeV/fm^3 . All quantities here have been multiplied by $(T_c/T)^4$ to map out the scaling properties with temperature T .

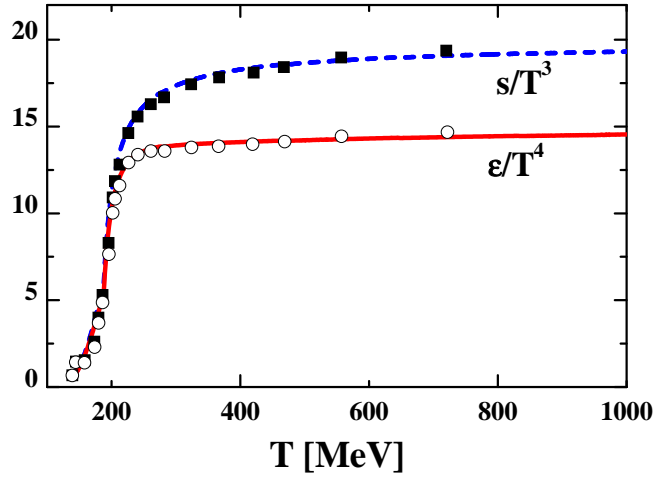


Fig. 4. The entropy density $s(T)$ (dashed line) and energy density $\epsilon(T)$ (solid line) from the DQPM in comparison to the lQCD results from Ref. [22] (full squares and open dots).

perature. We briefly note that the agreement is sufficiently good. This also holds for the 'equation of state', i.e. P/ϵ versus ϵ as demonstrated in Fig. 5.

As discussed in detail in Refs. [20,21] and explicitly addressed in Eq. (7), the energy-density functional can be separated in space-like and time-like sectors when the spectral functions acquire a finite width. The space-like (-) part of (7)

$$V_p(T, \mu_q) = T_{g-}^{00} + T_{q-}^{00} + T_{\bar{q}-}^{00} \quad (12)$$

may be interpreted as a potential-energy density V_p since the field quanta involved are virtual and correspond to partons exchanged in interaction diagrams. The time-like part (+) of (7) corresponds to effective field quanta which can be propagated within the light-cone. Without repeating the details we mention that mean-field

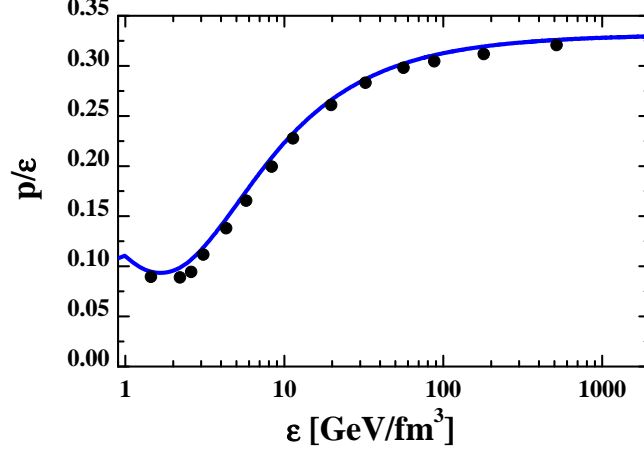


Fig. 5. The equation-of-state (solid line) from the DQPM in comparison to the IQCD results from Ref. [22] (full dots).

potentials for partons can be defined by the derivative of the potential-energy density V_p with respect to the time-like parton densities and effective interactions by second derivatives of V_p (cf. Section 3 in Ref. [21]).

In analogy to relativistic effective approaches for nucleonic degrees of freedom [34,35] we assume the potential energy density (12) to be a sum of scalar and vector parts, i.e.

$$V_p(T, \mu_q) = V_s(T, \mu_q) + V_v(T, \mu_q) . \quad (13)$$

In the dynamical quasi-particle picture the pressure P then is a sum of kinetic as well as interaction parts, i.e.

$$P(T, \mu_q) = \langle P_{xx} \rangle_{T, \mu_q} - V_s(T, \mu_q) + V_v(T, \mu_q) \quad (14)$$

with

$$\langle P_{xx} \rangle_{T, \mu_q} = \frac{1}{3} \left(Tr_g^+ \left(\frac{\mathbf{p}^2}{\omega} \right) + Tr_q^+ \left(\frac{\mathbf{p}^2}{\omega} \right) + Tr_{\bar{q}}^+ \left(\frac{\mathbf{p}^2}{\omega} \right) \right) . \quad (15)$$

In a similar way the total energy density ϵ can be expressed as

$$\epsilon(T, \mu_q) = \langle \omega \rangle_{T, \mu_q} + V_s(T, \mu_q) + V_v(T, \mu_q) \quad (16)$$

with the time-like quasiparticle energy density given by

$$\langle \omega \rangle_{T, \mu_q} = Tr_g^+ (\omega) + Tr_q^+ (\omega) + Tr_{\bar{q}}^+ (\omega) . \quad (17)$$

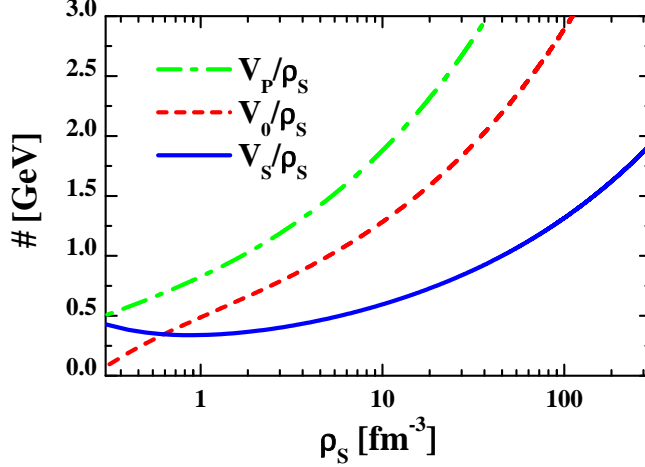


Fig. 6. The total potential energy per scalar parton (green dashed-dotted line) separated into scalar (solid blue line) and vector (red dashed line) parts (see text) as a function of the scalar parton density ρ_s .

Note the different signs for the scalar interaction part in (14) and (16) which stem from the metric tensor in the energy-momentum tensor $T^{\mu\nu}$. Since the total energy density as well as pressure are known in the DQPM and the kinetic parts (15) and (16) can be evaluated as well, the vector and scalar interaction densities can be uniquely extracted from the equations above. The corresponding results are displayed in Fig. 6 for the total interaction per scalar particle V_p/ρ_s (upper dot-dashed line) and its decomposition in scalar (solid line) and vector (dashed line) parts as a function of the scalar parton density ρ_s ,

$$\rho_s = \rho_g^s + \rho_q^s + \rho_{\bar{q}}^s, \quad (18)$$

which is a convenient (Lorentz invariant) quantity to characterize the system instead of the Lagrange parameters T^{-1} and μ_q . In fact, as found in Ref. [19] the thermodynamic quantities for different T and μ_q are very close when representing them as a function of ρ_s or the parton density $\rho_p = N_g^+ + N_q^+ + N_{\bar{q}}^+$, respectively.

Scalar and vector mean-field potentials are defined by derivatives of V_s and V_v with respect to the densities ρ_s and ρ_v , respectively,

$$U_s(\rho_s) = \frac{\partial V_s}{\partial \rho_s}; \quad U_v^0 = \frac{\partial V_v}{\partial \rho_p}. \quad (19)$$

Both quantities (after differentiation) may be considered as a function of the parton-scalar density ρ_s . The resulting functions are displayed in Fig. 7 as a function of ρ_s and show approximately equal results at high scalar density (or energy density, respectively). The low-density properties, however, are very different. Whereas the vector-mean field drops to zero with decreasing ρ_s the scalar-mean field increases substantially below $\rho_s \approx 1 \text{ fm}^{-3}$; it very smoothly increases with density for $\rho_s > 2$

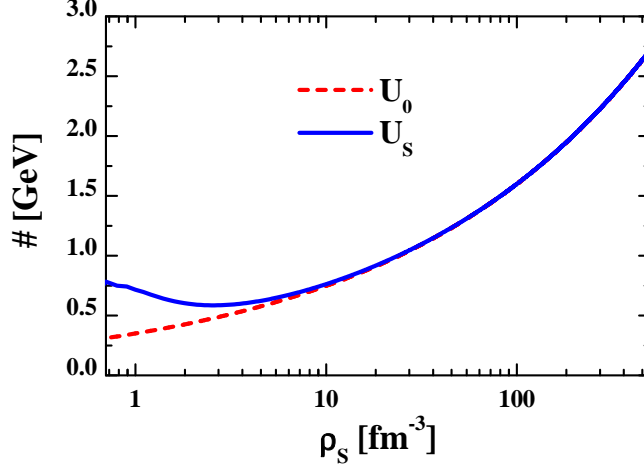


Fig. 7. The scalar (blue solid line) and vector (red dashed line) mean-fields for quarks (19) as a function of the scalar parton density ρ_s .

fm^{-3} ¹. Accordingly scalar forces on the partons $\sim -\partial U_s/\partial\rho_s\nabla\rho_s$ are rather small in the high-density partonic phase and only become strong in the low-density phase close to hadronization. The DQPM as well as lQCD do not allow to extrapolate U_s down to $\rho_s = 0$ reliably but one might imagine that $U_s(\rho_s \rightarrow 0) \rightarrow \infty$ thus encoding scalar confinement on the mean-field level. We note that in actual PHSD calculations such low partonic densities are not probed dynamically because the partons hadronize in the region $\rho_s \approx 1$ to 2 fm^{-3} (see below).

With the scalar- and vector-mean fields fixed for the partons (assuming the gluon mean fields to be twice the quark mean fields according to the analysis within the DQPM (cf. Ref. [21]) and with the effective masses and dynamical widths fixed by the DQPM (as a function of ρ_s instead of (T/T_c)) the mean-field propagation of partons in PHSD is fully determined by the off-shell transport equations (cf. the review [19]). However, the elastic and inelastic cross sections of quarks and gluons, which enter the collision terms, have to be specified separately.

2.2 Elastic and inelastic parton scattering

On the partonic side the following elastic and inelastic interactions are included $qq \leftrightarrow qq$, $\bar{q}\bar{q} \leftrightarrow \bar{q}\bar{q}$, $gg \leftrightarrow gg$, $gg \leftrightarrow g$, $q\bar{q} \leftrightarrow g$ exploiting 'detailed-balance' with interaction rates from the DQPM [4,20,21]. Since the parameters of the DQPM have been updated, a recalculation for the effective cross sections has been necessary. Since the explicit procedure is going along with a few approximations - subject to debate - we prefer to show the actual cross sections employed in PHSD which are about a factor of two smaller than those presented in Ref. [14] before due to the lower reaction rates encoded in the width γ_g .

¹ Note the logarithmic scale in ρ_s .

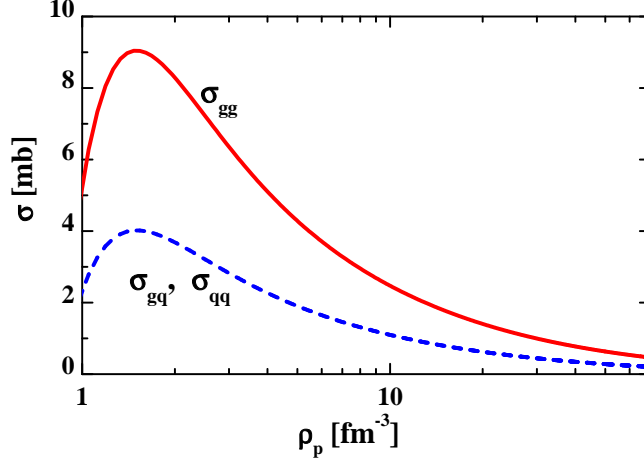


Fig. 8. The effective gluon-gluon \rightarrow gluon-gluon (red solid line), gluon-quark \rightarrow gluon-quark and quark-quark \rightarrow quark-quark (blue dashed line) cross section from the DQPM as a function of the scalar parton density ρ_s .

The actual values for elastic gg scattering are shown in Fig. 8 as a function of the scalar parton density ρ_s (solid line) and demonstrate that gg cross sections up to 10 mb can be reached at $\rho_s \approx 2 \text{ fm}^{-3}$. The effective cross section drops rapidly with increasing ρ_s which signals that weakly interacting partons show up at very high parton density. Some note of caution has to be added here since though the cross section σ_{gg} drops with ρ_s the collision rate of a gluon ($\sim \sigma_{gg}\rho_p$) increases slightly with ρ_s . For quark-quark or quark-antiquark elastic scattering the cross section is reduced by a factor 4/9 in line with Casimir scaling [23,24]. Quark-gluon elastic scattering (in the present implementation) is also reduced by a factor 4/9 (cf. Fig. 8, dashed line).

The channels $q\bar{q} \rightarrow g$ are described by a relativistic Breit-Wigner cross section as a function of the invariant energy \sqrt{s}

$$\sigma_{q\bar{q} \rightarrow g}(\sqrt{s}) = \frac{2}{4} \frac{\pi}{k^2} \frac{s\gamma_g^2}{(s - M^2)^2 + s\gamma_g^2} \hat{B}, \quad (20)$$

which is determined by the actual masses of the fermions $M_q, M_{\bar{q}}$ and the resonance parameters of the gluon (M_g, γ_g) at fixed scalar density ρ_s (from the DQPM). The factor k^2 in (20) is given by

$$k^2 = (s - (M_q + M_{\bar{q}})^2)(s - (M_q - M_{\bar{q}})^2)/(4s), \quad (21)$$

and the prefactor 2/4 stands for the spin-factor assuming two transverse gluon degrees of freedom. Note that for two initial spin-1/2 fermions we get $(2s + 1)^2 = 4$. The factor \hat{B} in (20) stands for the branching ratio which is the partial width for gluon decay to quark+antiquark relative to the total width γ_g . Since γ_g describes the total reaction rate of gluons at fixed density ρ_s (or temperature T) the latter

may approximately be determined by the transport calculations in equilibrium (i.e. within a box employing periodic boundary conditions). Our studies give $\hat{B} \approx 0.8$ which will be used furtheron. In PHSD a further constraint on flavor neutrality and open color is employed to ensure that no 'color neutral' or flavored gluons occur. The gluon decay to a $u\bar{u}, d\bar{d}$ or $s\bar{s}$ pair is fixed by detailed balance. We have to mention here that the strange quarks are about 50 MeV heavier than the light u, d quarks, i.e. $M_s = M_u + 50$ MeV, which slightly suppresses the gluon decay to $s\bar{s}$ relative to $u\bar{u}$ or $d\bar{d}$.

Further channels incorporated are $gg \leftrightarrow g$ which are given by Breit-Wigner cross sections (with the gluon resonance parameters) and detailed balance, respectively, but not specified explicitly due to their low impact in the actual calculations (even when assuming a branching ratio close to unity).

2.3 Hadronization in PHSD

The hadronisation, i.e. the transition from partonic to hadronic degrees of freedom, is described in PHSD by local covariant transition rates as introduced in Ref. [14] e.g. for $q + \bar{q}$ fusion to a meson m of four-momentum $p = (\omega, \mathbf{p})$ at space-time point $x = (t, \mathbf{x})$:

$$\begin{aligned} \frac{dN_m(x, p)}{d^4x d^4p} &= Tr_r q Tr_r \bar{q} \delta^4(p - p_q - p_{\bar{q}}) \delta^4\left(\frac{x_q + x_{\bar{q}}}{2} - x\right) \\ &\times \omega_q \rho_q(p_q) \omega_{\bar{q}} \rho_{\bar{q}}(p_{\bar{q}}) |v_{q\bar{q}}|^2 W_m(x_q - x_{\bar{q}}, (p_q - p_{\bar{q}})/2) \\ &\times N_q(x_q, p_q) N_{\bar{q}}(x_{\bar{q}}, p_{\bar{q}}) \delta(\text{flavor, color}). \end{aligned} \quad (22)$$

In Eq. (22) we have introduced the shorthand notation,

$$Tr_j = \sum_j \int d^4x_j \int \frac{d^4p_j}{(2\pi)^4}, \quad (23)$$

where \sum_j denotes a summation over discrete quantum numbers (spin, flavor, color); $N_j(x, p)$ is the phase-space density of parton j at space-time position x and four-momentum p . In Eq. (22) $\delta(\text{flavor, color})$ stands symbolically for the conservation of flavor quantum numbers as well as color neutrality of the formed hadron m which can be viewed as a color-dipole or 'pre-hadron'. Furthermore, $v_{q\bar{q}}(\rho_p)$ is the effective quark-antiquark interaction from the DQPM (displayed in Fig. 10 of Ref. [21]) as a function of the local parton ($q + \bar{q} + g$) density ρ_p (or energy density). Furthermore, $W_m(x, p)$ is the dimensionless phase-space distribution of the formed 'pre-hadron', i.e.

$$W_m(\xi, p_\xi) = \exp\left(\frac{\xi^2}{2b^2}\right) \exp\left(2b^2(p_\xi^2 - (M_q - M_{\bar{q}})^2/4)\right) \quad (24)$$

with $\xi = x_1 - x_2 = x_q - x_{\bar{q}}$ and $p_\xi = (p_1 - p_2)/2 = (p_q - p_{\bar{q}})/2$ (which has been previously introduced in Eq. (2.14) of Ref. [36]). The width parameter b is fixed by $\sqrt{\langle r^2 \rangle} = b = 0.66$ fm (in the rest frame) which corresponds to an average rms radius of mesons. We note that the expression (24) corresponds to the limit of independent harmonic oscillator states and that the final hadron-formation rates are approximately independent of the parameter b within reasonable variations. By construction the quantity (24) is Lorentz invariant; in the limit of instantaneous 'hadron formation', i.e. $\xi^0 = 0$, it provides a Gaussian dropping in the relative distance squared $(\mathbf{r}_1 - \mathbf{r}_2)^2$. The four-momentum dependence reads explicitly (except for a factor $1/2$)

$$(E_1 - E_2)^2 - (\mathbf{p}_1 - \mathbf{p}_2)^2 - (M_1 - M_2)^2 \leq 0 \quad (25)$$

and leads to a negative argument of the second exponential in (24) favoring the fusion of partons with low relative momenta $p_q - p_{\bar{q}} = p_1 - p_2$.

In principle the two-particle Green's-function, $G^<(x_q, p_q, x_{\bar{q}}, p_{\bar{q}})$, should appear in Eq. (22). However, the approximation of the two-particle Green's function by a product of single-particle Greens functions (in case of different particles) is always a first step in a cluster expansion for Green's functions and neglects 'residual correlations' stemming from higher order contractions. The same holds for an approximation of the three-particle Green's function by the (symmetrized/antisymmetrized) product of single-particle Green's functions (cf. Ref. [37]). On the other hand, the DQPM with its dynamical spectral functions already includes the effects of strong two-body correlations - contrary to bare Green's functions - such that the effect of residual interactions might be discarded in a first approximation.

Related transition rates (to Eq. (22)) are defined for the fusion of three off-shell quarks ($q_1 + q_2 + q_3 \leftrightarrow B$) to a color neutral baryonic (B or \bar{B}) resonances of finite width (or strings) fulfilling energy and momentum conservation as well as flavor current conservation, i.e.

$$\begin{aligned} \frac{dN_B(x, p)}{d^4x d^4p} &= Tr_{q_1} Tr_{q_2} Tr_{q_3} \delta^4(p - p_{\xi_3}) \delta^4(x - \xi_3) \delta(\sqrt{(\tau_1 - \tau_2)^2}) \\ &\times \omega_{q_1} \rho_{q_1}(p_1) \omega_{q_2} \rho_{q_2}(p_2) \omega_{q_3} \rho_{q_3}(p_3) \\ &\times |M_{qqq}|^2 W_B(\xi_1, \xi_2, p_{\xi_1}, p_{\xi_2}) \\ &\times N_{q_1}(x_1, p_1) N_{q_2}(x_2, p_2) N_{q_3}(x_3, p_3) \delta(\text{flavor, color}). \end{aligned} \quad (26)$$

In (26) the factor $\delta(\sqrt{(\tau_1 - \tau_2)^2})$ implies that the partons hadronize at the same time in the rest frame of the three-parton system. Furthermore, the quantity W_B denotes the dimensionless baryon phase-space distribution in the independent harmonic oscillator limit

$$W_B(\xi_1, \xi_2, p_{\xi_1}, p_{\xi_2}) = \exp\left(\left(\frac{1}{2}\xi_1^2 + \frac{2}{3}\xi_2^2\right)/\tilde{B}^2\right) \exp\left(\tilde{B}^2(2p_{\xi_1}^2 + \frac{3}{2}p_{\xi_2}^2)\right) \quad (27)$$

$$\times \exp\left(-\tilde{B}^2\left(\frac{1}{2}(M_1 - M_2)^2 + \frac{1}{6}(M_1 + M_2 - 2M_3)^2\right)\right)$$

evaluated in Jacobi coordinates

$$\xi_1 = x_1 - x_2, \quad \xi_2 = \frac{x_1 + x_2}{2} - x_3, \quad \xi_3 = \frac{x_1 + x_2 + x_3}{3}, \quad (28)$$

$$p_{\xi_1} = \frac{p_1 - p_2}{2}, \quad p_{\xi_2} = \frac{1}{3}(p_1 + p_2 - 2p_3), \quad p_{\xi_3} = p_1 + p_2 + p_3.$$

The width parameter \bar{B} in (27) is taken as $\bar{B} = 1$ fm which corresponds to an average rms radius of excited baryons. For simplicity we have assumed all quark (or antiquark) masses M_i to be equal in (27) and the actual calculations. The matrix element squared $|M_{qqq}|^2$ reflects the strength of three-quark fusion processes and is fixed as follows (cf. Refs. [14,38]): Since Regge trajectories for excited mesonic and baryonic states have the same slope (or string constant in the color dipole picture) we set $|M_{qqq}|^2 = |v_{q\bar{q}}|^2$ in our present work which implies that (so far) there is no need to introduce any new parameters.

On the hadronic side PHSD includes explicitly the baryon octet and decouplet, the 0^- - and 1^- -meson nonets as well as selected higher resonances as in HSD [25,26]. Hadrons of higher masses (> 1.5 GeV in case of baryons and > 1.3 GeV in case of mesons) are treated as 'strings' (color-dipoles) that decay to the known (low-mass) hadrons according to the JETSET algorithm [39]. We discard an explicit recapitulation of the string decay and refer the reader to the original work [39] or Ref. [40].

2.4 Numerical realizations

As mentioned above, the dynamical evolution of the system is entirely described by the transport dynamics in PHSD incorporating the off-shell propagation of the partonic quasiparticles according to Refs. [16,17,19] as well as the transition to resonant hadronic states (or 'strings') Eqs. (22), (26). The time integration for the testparticle-equations of motion (cf. Refs. [17]) is performed in the same way as in case of hadronic off-shell transport where (in view of the momentum-independent width γ) the simple relation (19) in Ref. [41] is employed. For the collisions of partons two variants are at our disposal: i) geometrical collision criteria as employed in standard hadronic transport, ii) the in-cell method developed in Ref. [42]. The latter can easily be extended to describe $2 \leftrightarrow 3$ processes etc. in a covariant way [43] and is the better choice at high particle densities (cf. Ref. [44]) and actually used in the calculations presented below. The hadronization is performed by integrating the rate equations (22) and (26) in space and time which are discretized on a four-dimensional grid by Δt and $\Delta V(t) = \Delta x(t)\Delta y(t)\Delta z(t)$. In beam direction we use an initial grid size $\Delta z = 1/\gamma_{cm}$ fm with γ_{cm} denoting the Lorentz- γ factor in the nucleon-nucleon center-of-mass system while in the transverse direction we use $\Delta x = \Delta y = 1$ fm.

The grid size is increased dynamically during the transport calculation such that all particles are included on the actual grid. This practically implies that the grid boundary in beam direction approximately moves with the velocity of light. In each time step Δt and cell ΔV the integrals in (22) and (26) are evaluated by a sum over all (time-like) testparticles using (e.g. for the quark density)

$$\frac{1}{\Delta V} \int_{\Delta V} d^3x \int \frac{d\omega_q}{2\pi} \omega_q \int \frac{d^3p_q}{(2\pi)^3} \rho_q(\omega_q, p_q) N_q(x, p_q) = \frac{1}{\Delta V} \sum_{J_q \text{ in } \Delta V} 1 = \rho_q(\Delta V), \quad (29)$$

where the sum over J_q implies a sum over all testparticles of type q (here quarks) in the local volume ΔV in each parallel run. In case of other operators like the scalar density, energy density etc. the number 1 in Eq. (29) has to be replaced by $\sqrt{P_J^2}/\omega_J$, ω_J etc. In order to obtain lower numerical fluctuations the integrals are averaged over the number of parallel runs (typically a few hundred). For each individual testparticle (i.e. x_q and p_q fixed) the additional integrations in (22) and (26) give a probability for a hadronization process to happen; the actual event then is selected by Monte Carlo. Since energy-momentum conservation fixes the four-momentum p of the hadron produced - the space-time position x is determined by (22) or (26) - the latter is represented by a hadronic state with flavor content fixed by the fusing quarks (antiquarks) or by a string of invariant mass \sqrt{s} with fixed flavor content.

2.5 Initial conditions

The initial conditions for the parton/hadron dynamical system have to be specified additionally. In Ref. [14] we have considered an anisotropic ellipsoid in coordinate space with thermal energy distributions for the partons including the parton-spectral functions of finite width (fixed by the DQPM at initial temperature T_0). In order to describe relativistic heavy-ion reactions, however, one has to start with two nuclei in their 'semi-classical' groundstate, boosted towards each other with a velocity β (in z -direction), fixed by the bombarding energy. The initial phase-space distributions of the projectile and target nuclei are determined in the local Thomas-Fermi limit as in the HSD transport approach [25,26]. We recall that at moderate relativistic energies the initial interactions of two nucleons are well described by the excitation of two color-neutral strings which decay in time to the known hadrons (mesons, baryons, antibaryons) [39]. Hard processes are described (as in HSD) via PYTHIA 5.7 [45] and take into account short-range high-momentum transfer reactions that can well be described by perturbative QCD. The novel element in PHSD (relative to HSD) is the 'string melting concept' as also used in the AMPT model [11] in a similar context. However, in PHSD the strings (or possibly formed hadrons) are only allowed to 'melt' if the local energy density $\epsilon(x)$ (in the local rest frame) is above a transition energy density ϵ_c . The present DQPM version (fitted to the lQCD results from Ref. [22])

gives $\epsilon_c \approx 1.2 \text{ GeV/fm}^3$. The mesonic strings then decay to quark-antiquark pairs according to an intrinsic momentum distribution,

$$F(\mathbf{q}) \sim \exp(-2b^2\mathbf{q}^2) , \quad (30)$$

in the meson-rest frame (cf. Eq. (22) for the inverse process). The parton final four-momenta are selected randomly according to the momentum distribution (30) (with $b=0.66 \text{ fm}$), and the parton-energy distribution is fixed by the DQPM at given energy density ϵ in the local cell with scalar parton density ρ_s . The flavor content of the $q\bar{q}$ pair is fully determined by the flavor content of the initial string. By construction the 'string melting' to massive partons conserves energy and momentum as well as the flavor content. In contrast to Ref. [11] the partons are of finite mass - in line with their local spectral function - and obtain a random color $c = (1, 2, 3)$ or (r, b, g) in addition. Of course, the color appointment is color neutral, i.e. when selecting a color c for the quark randomly the color for the antiquark is fixed by $-c$.

In case of baryonic (antibaryonic) strings the latter first decay to a massive 'diquark' (using Jacobi coordinates) and a 3rd massive quark according to the momentum distribution

$$F_{dq}(\mathbf{q}) \sim \exp(-2\hat{B}^2\mathbf{q}^2) \quad (31)$$

in line with Eq. (26), while the diquark immediately decays to two further massive quarks in line with the momentum distribution specified in (24). This strategy ensures an approximate 'detailed-balance' for the local 'melting' and 'hadronization' processes. Once the partonic degrees of freedom are liberated (deconfined) they interact with the partonic cross sections (specified in Section 2.2) or hadronize as described in Section 2.3.

We mention that the concept of an initial hadron/string phase followed by a local partonic stage as well as a final hadronic phase has been adopted also by the authors of Refs. [46–48]. However, in the latter case the initial phase is described by UrQMD [49,50] (instead of HSD) and the local partonic stage is evolved by ideal hydrodynamics (instead of off-shell parton transport in PHSD). Furthermore, the conversion of the hydrodynamic fluid to hadrons is incorporated in a Cooper-Frye formalism (instead of covariant transition rates in PHSD). The final hadronic stage again is evolved by UrQMD (instead of HSD). Since both hadron/string transport approaches (HSD and UrQMD) yield very similar results for most of the non-strange hadrons, the model of Refs. [46–48] differs essentially in the hydrodynamical treatment of the partonic stage.

3 Application to nucleus-nucleus collisions

In this Section we employ the PHSD approach - described in Section 2 - to nucleus-nucleus collisions at moderate relativistic energies, i.e. at SPS energies where our initialization (see above) is expected to work. Note that at RHIC or LHC energies other initial conditions (e.g. a color-glass condensate [51]) might be necessary. Since this is a slightly different subject we here restrict to bombarding energies below 160 A·GeV where such problems/questions are expected to be not relevant.

3.1 Partonic energy fractions

We start with a consideration of energy partitions in order to map out the fraction of partonic energy in time for relativistic nucleus-nucleus collisions. In Fig. 9 we show the energy balance for a central (impact parameter $b=1$ fm) reaction of Pb+Pb at 158 A · GeV, i.e. at the top SPS energy. The total energy E_{tot} (upper line) - which at $t = 0$ is given by the energy of the colliding nuclei in the cms - is conserved throughout the reaction, i.e. in the partonic and hadronization phase as well as in the hadronic phase. This also provides a measure of the numerical accuracy achieved in the actual calculations that have been performed for 100 parallel runs. Whereas in the first ~ 3 fm/c the total energy is entirely contained in the impinging nucleons (including about 6 MeV per nucleon of binding energy) a rapid transition to partonic degrees of freedom is seen at $t \approx 3$ fm/c, i.e. when the nuclei have started to overlap and react. We recall that the transition time of the two Pb-nuclei is about $2R_{Pb}/\gamma_{cm} \approx 1.5$ fm/c at the top SPS energy. During this time period about 60% of initial kinetic energy of nucleons is converted to partons (red dashed line) and to mesons (short dashed green line) in the surface region ('corona') of the colliding system. Note that in the 'mesonic' energy E_m also 'unformed mesons' - as fragments of the strings - are accounted for. The energy of residual baryons (including antibaryons) is shown in terms of the dot-dashed (blue) line and is almost constant for $t > 5$ fm/c implying that the various final-state interactions do not show up significantly in the energy fractions. The partonic phase - in a limited space-time region - approximately ends for $t > 9$ fm/c which means that the further time evolution of the system is essentially described by hadronic interactions (HSD). Note that a sizeable fraction of energy is asymptotically still contained in the baryons. Since the baryon-rest masses amount to an energy of about 449 GeV (including newly produced $B\bar{B}$ pairs) this implies that full stopping is not achieved in central Pb+Pb collisions at 158 A · GeV ².

Let's have a closer look at the 'particle' composition in time for this reaction. We concentrate on those species that carry the energy transferred during the collision to new degrees of freedom. In this respect we display in Fig. 10 the number of produced partons (solid red line), mesons (long dashed green line) and newly produced baryons

² This has been pointed out more than a decade before in Refs. [26,52]

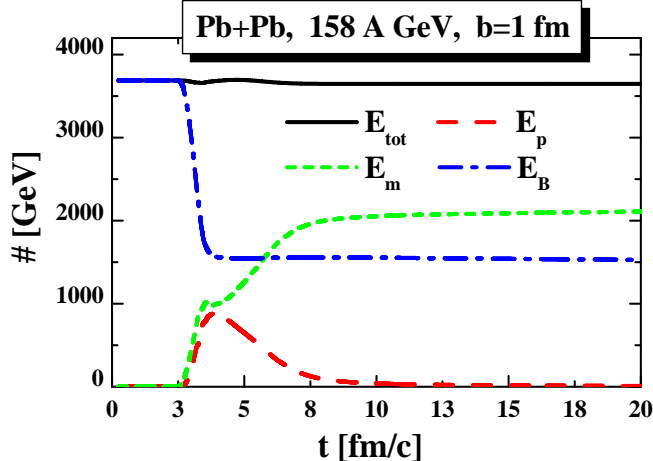


Fig. 9. The total energy E_{tot} (upper solid line) for central ($b=1$ fm) collisions of Pb+Pb at 158 A·GeV. The long-dashed (red) line shows the energy contributions E_p from partons while the short-dashed (green) line displays the energy contribution from mesons E_m (including 'unformed mesons' in strings). The dot-dashed (blue) line is the contribution of baryons (and antibaryons) E_B ; the difference between the initial baryonic energy $E_B(t=0)$ and final baryonic energy $E_B(t \rightarrow \infty)$ gives the energy that is converted during the heavy-ion collision to final mesonic states.

+ antibaryons (blue dashed line) as a function of time for the same reaction as before. We recall that the initial number of nucleons is 416 in this case. Slightly more than 1500 partons are produced during the passage time of the nuclei which disappear practically after 9 fm/c and essentially form mesons. The number of newly produced $B+\bar{B}$ pairs is small at this energy but its flavor decomposition is quite interesting (see below). An essential point here is that the number of final hadronic states is larger than the number of partons, i.e. there is a production of entropy in the hadronization process as pointed out before in Ref. [14]³ This implies that in PHSD the second law of thermodynamics is not violated in the hadronization process!

In order to shed more light on the hadronization process in PHSD we display in Fig. 11 the invariant mass distribution of $q\bar{q}$ pairs (solid line) as well as qqq (and $\bar{q}\bar{q}\bar{q}$) triples (dashed line) that lead to the formation of final hadronic states. The reaction is again Pb+Pb at 158 A·GeV. In fact, the distribution for the formation of baryon (antibaryon) states starts above the nucleon mass and extends to high invariant mass covering the nucleon resonance mass region as well as the high-mass continuum (which is treated by the decay of strings within the JETSET model [39,40]). On the 'pre-mesonic' side the invariant-mass distribution starts above the pion mass and extends up to continuum states of high invariant mass (described again in terms of string excitations). The low-mass sector is dominated by ρ , a_1 , ω or K^* , \bar{K}^* transitions etc. As mentioned before the excited 'pre-hadronic' states decay to two or more 'pseudoscalar octet' mesons such that the number of final hadrons is larger than the initial number of fusing partons.

³ Actually, the ratio of the maximum parton number to the final meson number is very close to the model studies in Ref. [14].

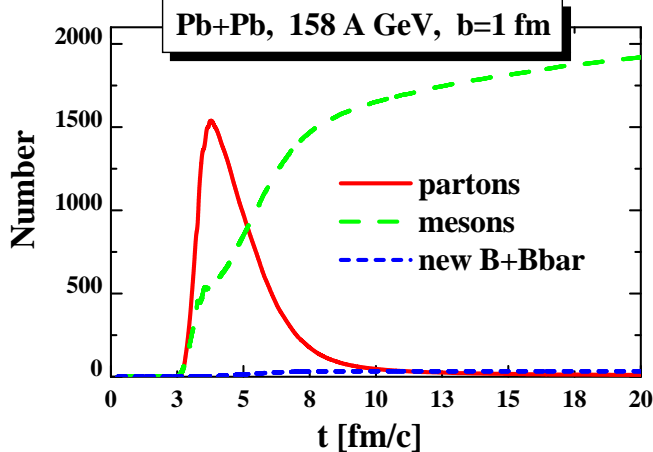


Fig. 10. The number of produced partons (solid red line), mesons (long dashed green line) and newly produced baryon + antibaryons (blue dashed line) as a function of time for Pb+Pb at 158 A·GeV (for $b=1$ fm). Note that the number of mesons still increases for $t > 20$ fm/c due to the decay of vector mesons etc.

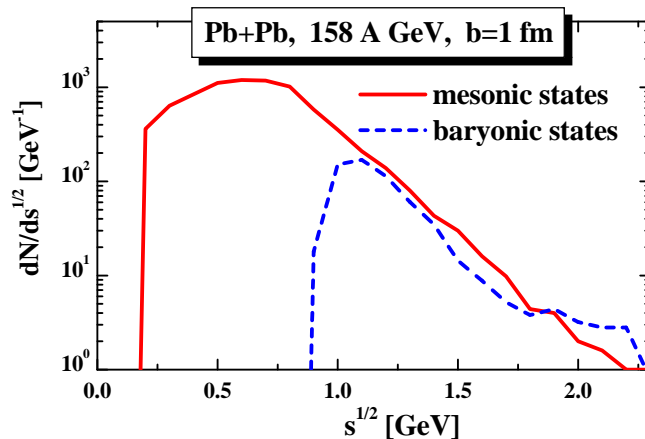


Fig. 11. The invariant mass distribution for fusing $q\bar{q}$ pairs (solid line) as well as qqq (and $\bar{q}\bar{q}\bar{q}$) triples (dashed line) that lead to the formation of final hadronic states for Pb+Pb collisions at 158 A·GeV ($b=1$ fm). Note that the high \sqrt{s} part suffers from sufficient statistics.

So far we have considered very central collisions that show a sizeable fraction of space-time regions of partonic nature but also of the hadronic (or string-like) corona. The question emerges to what extent the partonic phase shows up as a function of centrality. To this aim we study the partonic energy $E_p(b)$ relative to the energy converted from the kinetic motion of the impinging nuclei at impact parameter b , i.e.

$$R_p(b) = \frac{E_p(b)}{E_B(t=0, b) - E_B(t \rightarrow \infty, b)}, \quad (32)$$

which is displayed in Fig. 12 for impact parameter b from 1 fm to 13 fm in steps of 2

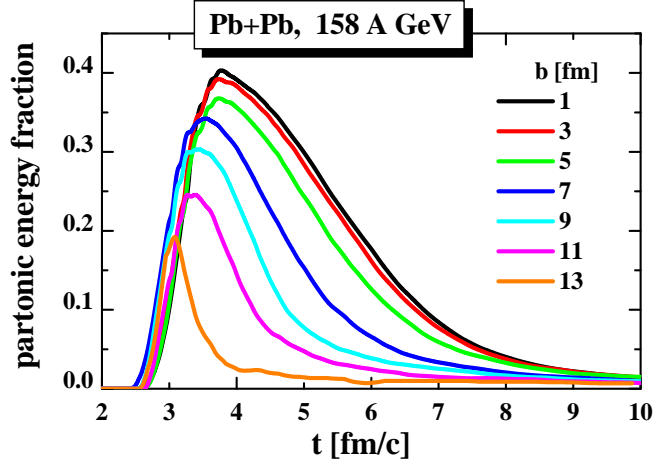


Fig. 12. The partonic energy fraction (defined by Eq. (32)) as a function of time for impact parameters b from 1 fm to 13 fm in steps of 2 fm. The system is Pb+Pb at 158 A·GeV.

fm. The system is again Pb+Pb at 158 A·GeV. One observes that even at very central collisions the partonic energy fraction (32) only reaches about 40% and decreases to about 20% (in the peak) for very peripheral reactions. More striking is the fact that the duration of the partonic phase shrinks substantially when going from central to peripheral reactions. Thus the 'popular picture' that a partonic phase is reached in the overlap region of the nuclei at top SPS energies is by far not substantiated by the PHSD calculations. This has been pointed out before in Refs. [53,54].

We continue with the ratio (32) as a function of bombarding energy concentrating here on the FAIR and full SPS energy regime but considering only central collisions ($b = 1$ fm). The results are displayed in Fig. 13 for central Pb+Pb collisions at 160, 80, 40, and 20 A·GeV as a function of time and demonstrate that the average duration of the partonic phase does not change very much with bombarding energy, however, the partonic volume shrinks by about a factor of three when stepping down in bombarding energy from 160 to 20 A·GeV. Thus according to our PHSD calculations there should be a QGP also at FAIR energies but its space-time volume is significantly smaller than that for the hadronic phase. At first sight this looks discouraging, but one should concentrate on observables with a special sensitivity to the partonic phase.

3.2 Particle spectra in comparison to experiment

Apart from the more general considerations in the previous Subsection, it is of interest, how the PHSD approach compares to the HSD model (without explicit partonic degrees of freedom) as well as to experimental data. We start with proton rapidity distributions at SPS that demonstrate the amount of initial baryon stopping and thus control the energy transfer in relativistic nucleus-nucleus collisions. Since we find the HSD results for the proton rapidity distribution dN/dy to be identical with

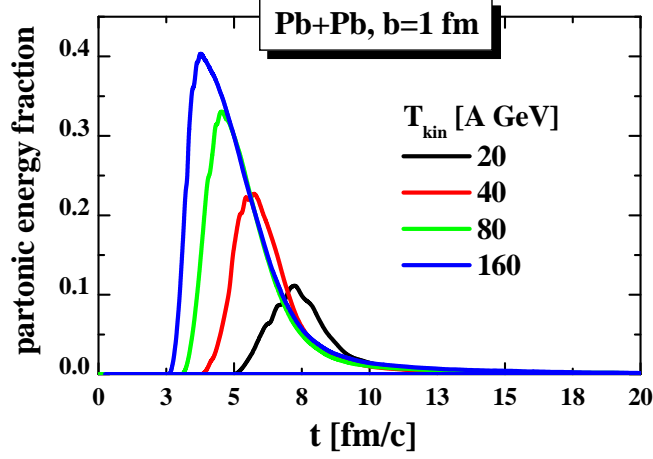


Fig. 13. The partonic energy fraction (defined by Eq. (32)) as a function of time for impact parameter $b = 1$ fm for Pb+Pb at 160, 80, 40 and 20 A·GeV.

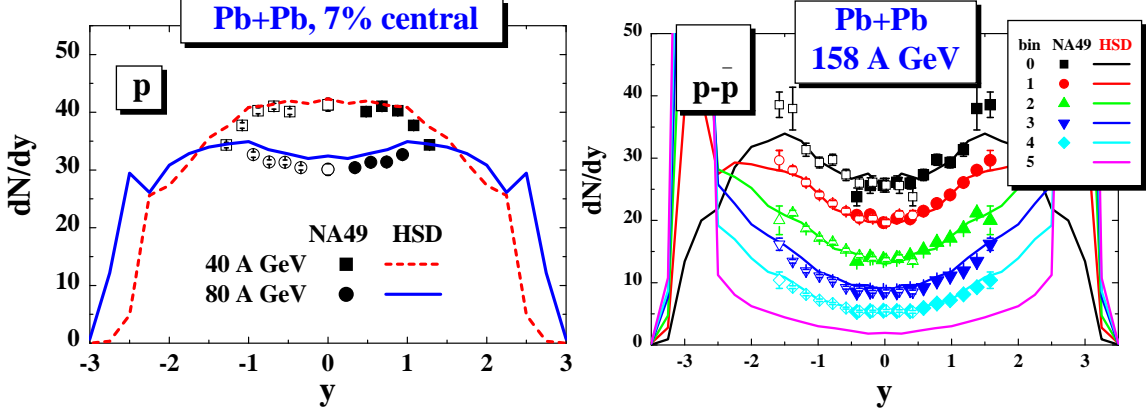


Fig. 14. The proton rapidity distributions for central (7%) Pb+Pb collisions at 40 and 80 (l.h.s.) in comparison to the data from Ref. [55]. The r.h.s. of the figure presents the net-proton rapidity distribution at 158 A·GeV for different centrality bins (bin 0 – 0-5%; bin 1 – 5-12%; bin 2 – 12.5-23.5%; bin 3 – 23.5-33.5%; bin 4 – 33.5-43.5% and bin 5 – 43.5-78.5% central events) from PHSD (solid lines) in comparison to the preliminary experimental data from the NA49 Collaboration [56].

the PHSD results (within statistics) we will only compare PHSD calculations to data of the NA49 Collaboration. Accordingly, in Fig. 14 the proton rapidity distributions from PHSD are compared to the data from Ref. [55] for 7% central Pb+Pb collisions at 40 and 80 A·GeV (l.h.s.). The r.h.s. of Fig. 14 shows the net-proton dN/dy from PHSD for 158 A·GeV Pb+Pb collisions for different centrality bins (bin 0 – 0-5%; bin 1 – 5-12%; bin 2 – 12.5-23.5%; bin 3 – 23.5-33.5%; bin 4 – 33.5-43.5% and bin 5 – 43.5-78.5% central events) in comparison to the preliminary experimental data [56]. In fact, the PHSD results demonstrate that the baryon stopping is reasonably reproduced in Pb+Pb collisions as a function of bombarding energy and centrality of the reaction.

Since the energy is dominantly transferred to mesons, which asymptotically appear as pions and kaons, we continue with pion and K^\pm rapidity distributions for 7%

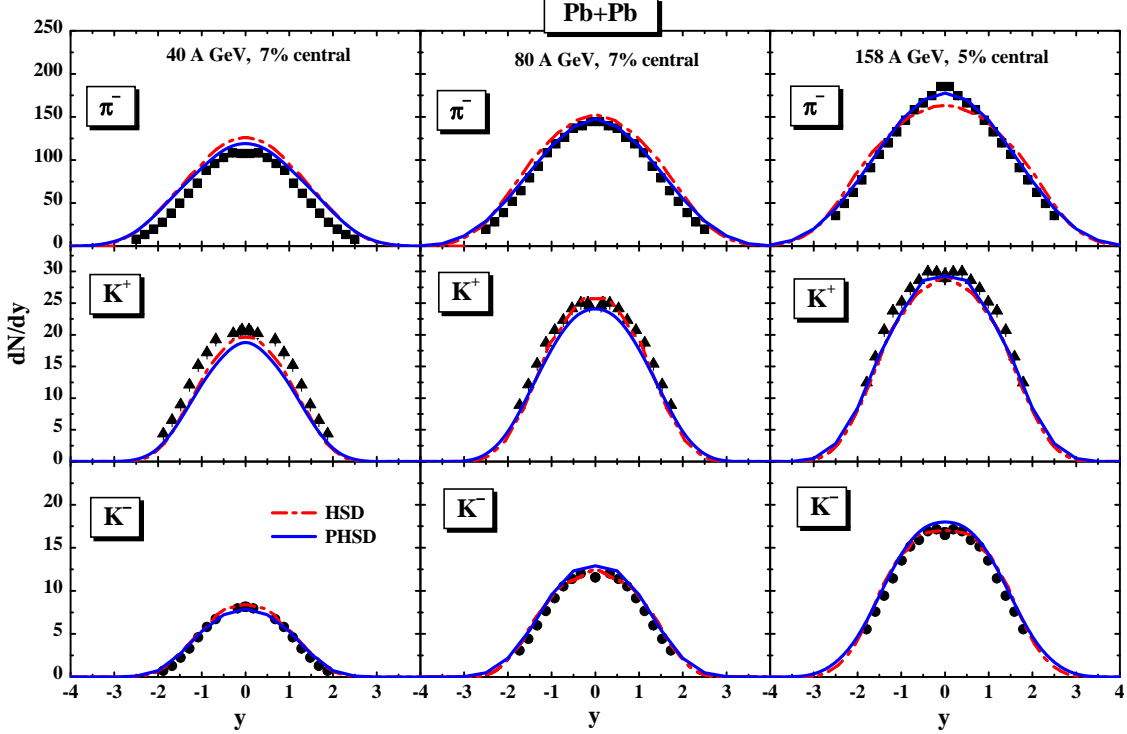


Fig. 15. The rapidity distribution of π^- (upper part), K^+ (middle part) and K^- (lower part) for 7% or 5% central Pb+Pb collisions at 40, 80 and 158 A·GeV from PHSD (solid blue lines) in comparison to the distribution from HSD (dashed red lines) and the experimental data from the NA49 Collaboration [57].

central Pb+Pb collisions at 40 and 80 A·GeV and 5% central collisions at 158 A·GeV since here rather complete data sets are available from the experimental side [57]. The results from PHSD (solid blue lines) are compared in Fig. 15 with the corresponding results from HSD (dashed red lines) and the experimental data for the same centralities in comparison to the rapidity spectrum from HSD (dashed red lines) and the experimental data from the NA49 Collaboration [57]. The actual deviations between the PHSD and HSD spectra are very moderate; the π^- rapidity distribution is slightly squeezed in width (in PHSD) and shows a more pronounced peak at midrapidity (at 158 A·GeV) more in line with the data. Nevertheless, it becomes clear from Fig. 15 that the energy transfer - reflected in the light meson spectra - is rather well described by PHSD, which thus passes another test.

Fig. 15 demonstrates that the longitudinal motion is rather well understood within the transport approaches and dominated by initial string formation and decay. Actually, there is no sizeable sensitivity of the rapidity spectra to an intermediate partonic phase. But what about the transverse degrees of freedom?

The answer to this question is offered in Fig. 16 where we show the transverse mass spectra of π^- , K^+ and K^- mesons for 7% central Pb+Pb collisions at 40 and 80 A·GeV and 5% central collisions at 158 A·GeV in comparison to the data of the NA49 Collaboration [57]. Here the slope of the π^- spectra is only slightly enhanced in PHSD

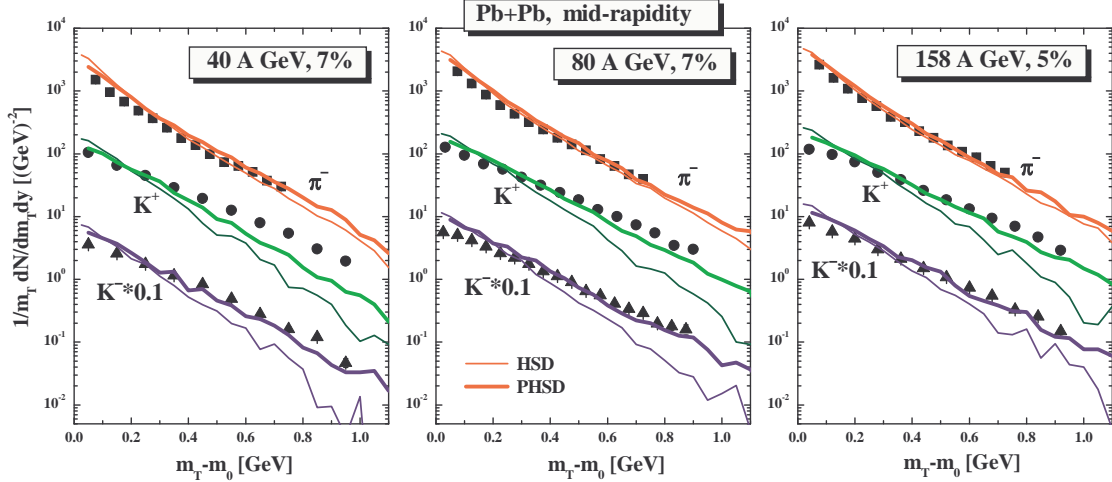


Fig. 16. The π^- , K^+ and K^- transverse mass spectra for central Pb+Pb collisions at 40, 80 and 158 A·GeV from PHSD (thick solid lines) in comparison to the distributions from HSD (thin solid lines) and the experimental data from the NA49 Collaboration [57].

(thick solid lines) relative to HSD (thin solid lines) which demonstrates that the pion transverse mass also show no sizeable sensitivity to the partonic phase. However, the K^\pm transverse mass spectra are substantially hardened with respect to the HSD calculations at all bombarding energies - i.e. PHSD is more in line with the data - and thus suggest that partonic effects are better visible in the strangeness-degrees of freedom. The hardening of the kaon spectra can be traced back to parton-parton scattering as well as a larger collective acceleration of the partons in the transverse direction due to the presence of repulsive vector fields for the partons. Note that the latter generate a Lorentz force very similar to that for nucleons in low-energy heavy-ion physics at SIS energies (< 2 A·GeV). The enhancement of the spectral slope for kaons and antikaons in PHSD due to collective partonic flow shows up much clearer for the kaons due to their significantly larger mass (relative to pions). We recall that in Refs. [58–60] the underestimation of the K^\pm slope by HSD (and also UrQMD) had been suggested to be a signature for missing partonic degrees of freedom. In fact, our present PHSD calculations support this early suggestion.

As a next step we focus on the strange baryons and show in Fig. 17 a comparison of PHSD rapidity spectra (blue solid lines) in comparison to HSD results (red dashed-dotted lines) and the experimental data from Ref. [61]. Here PHSD gives slightly lower $\Lambda + \Sigma^0$ yields for 7% central collisions of Pb+Pb at 40 and 80 A·GeV than HSD which demonstrates that PHSD is better in line with the data. At 158 A·GeV we find no significant difference between PHSD and HSD and slightly overshoot the experimental spectra from Ref. [61]. Note, however, that the rather flat rapidity distribution is well reproduced in shape. On the other hand there is a more recent data point from NA49 at midrapidity [62](green full square) for 5% central collisions which is higher due to a cut on more central reactions.

The strange antibaryon sector is of further interest since here the HSD calculations have always underestimated the yield [63]. Accordingly, we present the PHSD results

for the $\bar{\Lambda} + \bar{\Sigma}^0$ rapidity distributions in Fig. 18 for 7% or 10% central Pb+Pb collisions at 40, 80 and 158 A·GeV and additionally compare to the experimental data from the NA49 Collaboration [61,62]. Now PHSD slightly overestimates the experimental $\bar{\Lambda} + \bar{\Sigma}^0$ yield which is essentially due to a slightly enhanced production of strange baryon-antibaryon pairs in the hadronization phase described by Eq. (26). The full square at $y = 0$ corresponds to the recent 5% central data point from Ref. [62]. We tentatively attribute the sizeable $\bar{\Lambda} + \bar{\Sigma}^0$ yield to the presence of a partonic phase (as suggested already in 1982 by Rafelski and Müller [64]), which is underestimated in the HSD calculations as demonstrated by the (red) dot-dashed line in Fig. 18 (r.h.s.).

In order to examine this conjecture furthermore we show in Fig. 19 the Ξ^- rapidity distributions from PHSD (blue solid lines) in comparison to the NA49 data [61,62] and (at 158 A·GeV) to the results from HSD (red dot-dashed line). The Ξ^- baryons are dominantly produced by strangeness-exchange reactions $\bar{K}\Lambda \leftrightarrow \pi\Xi^-(\Xi^0)$ and $\bar{K}\Sigma \leftrightarrow \pi\Xi^-(\Xi^0)$ (where $\bar{K} = (K^-, \bar{K}^0)$) in the HSD and PHSD approaches. The cross sections for these (strange quark exchange) reactions have been taken from the predictions of the coupled-channel approach from Ref. [66] - based on a flavor SU(3)-invariant hadronic Lagrangian - which have been parametrized in Ref. [67]. As seen from Fig. 19, the double strange baryons (Ξ^-, Ξ^0) exhibit no significant enhancement from the partonic phase relative to HSD. Accordingly the Ξ^- yield is not a critical observable for a partonic stage.

This situation changes for double antistrange baryons: in Fig. 20 we present the PHSD rapidity spectra of $\bar{\Xi}^+$ for 7% or 10% central reactions of Pb+Pb at 40, 80 and 158 A·GeV by the solid (blue) lines, respectively. Indeed, the PHSD description of the data now is sufficiently good contrary to the HSD calculations at 158 A·GeV (red dot-dashed line) which underestimate the data by a factor of about three. This

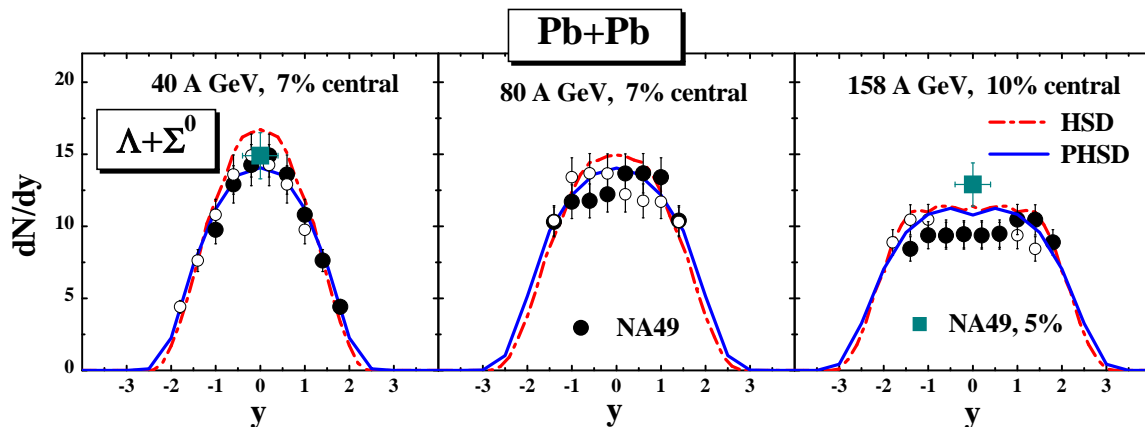


Fig. 17. The $\Lambda + \Sigma^0$ rapidity distributions for 7% central Pb+Pb collisions at 40, 80 and 10% central Pb+Pb collisions at 158 A·GeV from PHSD (blue thick solid lines) in comparison to the distributions from HSD (red dashed-dotted lines) and the experimental data (solid dots) from the NA49 Collaboration [61] (the open circles correspond to data points reflected at midrapidity). The full (green) square at $y = 0$ corresponds to the recent 5% central data point from Ref. [62].

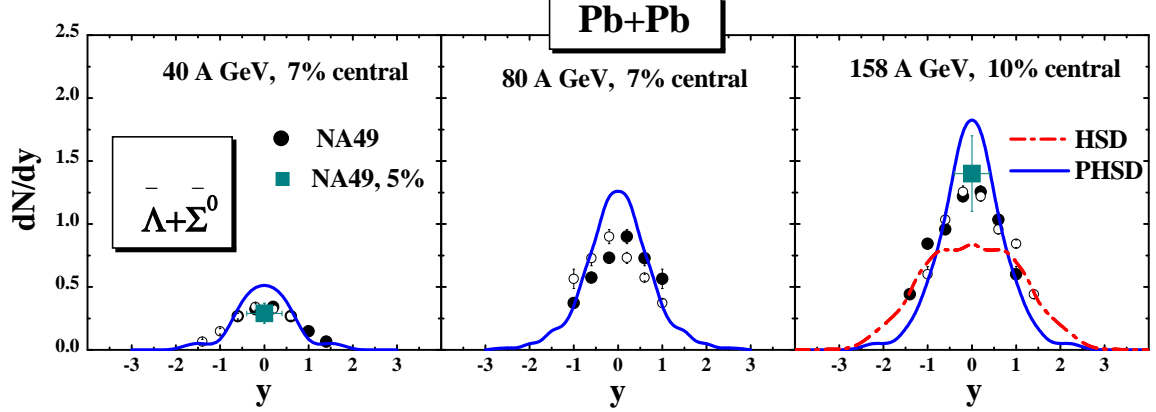


Fig. 18. The $\bar{\Lambda} + \bar{\Sigma}^0$ rapidity distributions for 7% central Pb+Pb collisions at 40, 80 and 10% central Pb+Pb collisions at 158 A·GeV from PHSD (blue thick solid lines) in comparison to the distribution from HSD (red dashed-dotted line for 158 A·GeV) and the experimental data from the NA49 Collaboration [61] (the open circles correspond to data points reflected at midrapidity). The full square at $y = 0$ corresponds to the recent 5% central data point from Ref. [62].

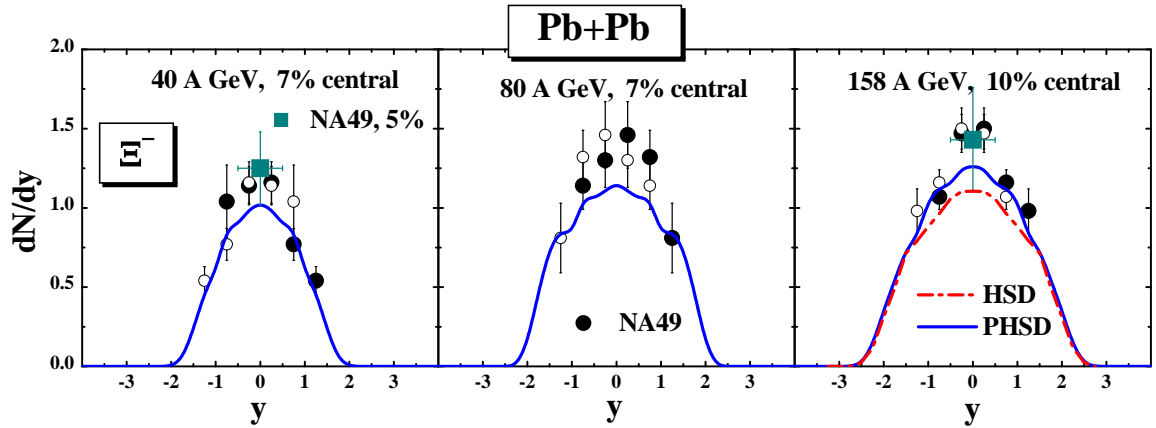


Fig. 19. The Ξ^- rapidity distributions for 7% central Pb+Pb collisions at 40, 80 and 10% central Pb+Pb collisions at 158 A·GeV from PHSD (blue thick solid lines) in comparison to the distribution from HSD (dashed-dotted line for 158 A·GeV) and the experimental data (circles) from the NA49 Collaboration [61] (the open circles correspond to data points reflected at midrapidity). The full square at $y = 0$ corresponds to the recent 5% central data point from Ref. [62].

observation points towards a partonic origin but needs further examination.

Independent experimental information is provided by the centrality dependence of the strange (and antistrange) baryon yield. In this respect we compare in Fig. 21 the multiplicities of $(\Lambda + \Sigma^0)/N_{wound}$ (l.h.s.) and $(\bar{\Lambda} + \bar{\Sigma}^0)/N_{wound}$ (r.h.s.) as a function of the number of wounded nucleons N_{wound} for Pb+Pb collisions at 158 A·GeV at mid-rapidity from PHSD (blue solid lines) and HSD (red dashed-dotted lines) to the experimental data from the NA57 Collaboration [65] (open triangles) and the NA49 Collaboration [62] (solid dots). The (green) full squares correspond to the 10% central data points at midrapidity from Ref. [61]. We mention that we employ the

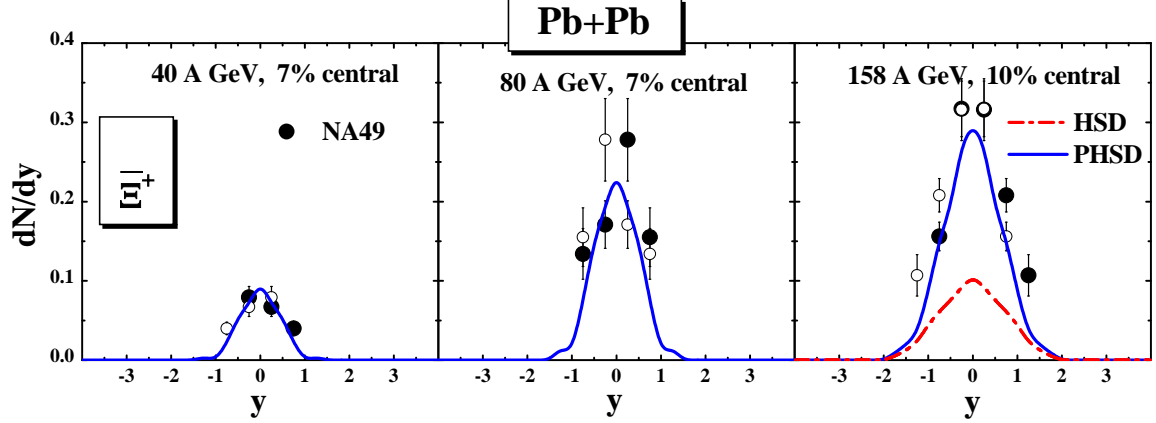


Fig. 20. The $\bar{\Xi}^+$ rapidity distributions for central Pb+Pb collisions at 40, 80 and 10% central Pb+Pb collisions at 158 A·GeV from PHSD (blue thick solid lines) in comparison to the distribution from HSD (red dashed-dotted line for 158 A·GeV) and the experimental data (circles) from the NA49 Collaboration [61] (the open circles correspond to data points reflected at midrapidity).

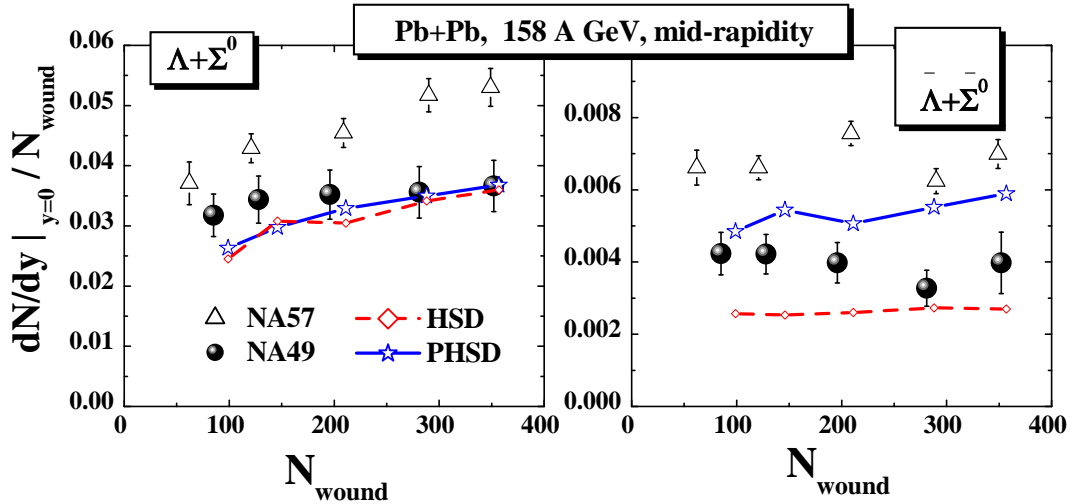


Fig. 21. The multiplicities of $(\Lambda + \Sigma^0)/N_{wound}$ (l.h.s.) and $(\bar{\Lambda} + \bar{\Sigma}^0)/N_{wound}$ (r.h.s.) as a function of the number of wounded nucleons N_{wound} for Pb+Pb collisions at 158 A·GeV at mid-rapidity from PHSD (blue solid lines) and HSD (red dashed-dotted lines) in comparison to the experimental data from the NA57 Collaboration [65] (open triangles) and the NA49 Collaboration [62] (solid dots). The HSD and PHSD calculations have an error of about 5–10% due to limited statistics.

same definition of wounded nucleons N_{wound} as the NA49 Collaboration. Whereas the HSD and PHSD calculations both give a reasonable description of the $\Lambda + \Sigma^0$ yield of the NA49 Collaboration, both models underestimate the NA57 data (open triangles) by about 30%. An even larger discrepancy in the data from the NA49 and NA57 Collaborations is seen for $(\bar{\Lambda} + \bar{\Sigma}^0)/N_{wound}$ (r.h.s.); here the PHSD calculations give results which are in between the NA49 data (solid dots) and the NA57 data (open triangles). We also see that HSD underestimates the $(\bar{\Lambda} + \bar{\Sigma}^0)$ midrapidity yield at all centralities in line with our findings before.

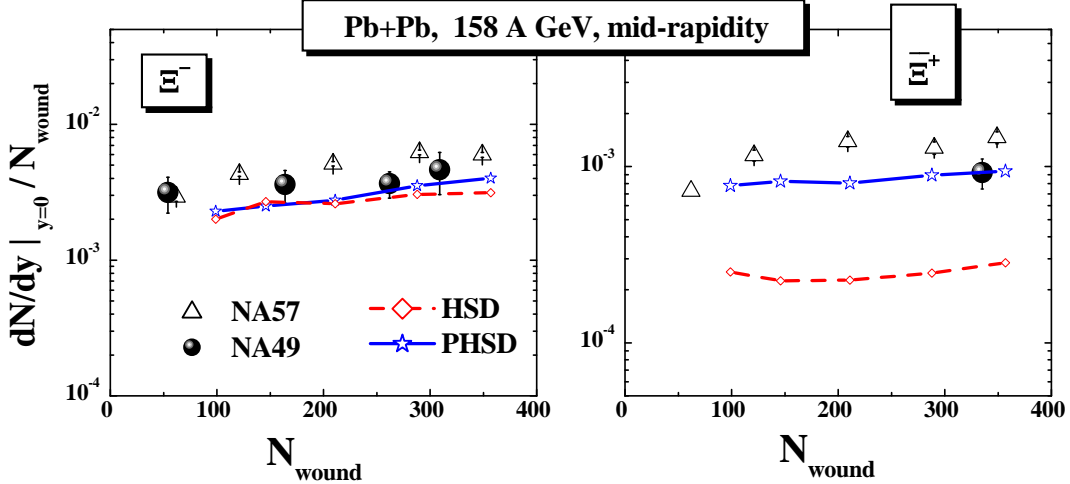


Fig. 22. The multiplicities of Ξ^-/N_{wound} (l.h.s.) and Ξ^+/N_{wound} (r.h.s.) as a function of wounded nucleons for Pb+Pb collisions at 158 A·GeV at mid-rapidity from PHSD (blue solid lines) and HSD (red dashed-dotted lines) in comparison to the experimental data from the NA57 Collaboration [65] (open triangles) and the NA49 Collaboration [61,62] (solid dots).

The latter results suggest that the partonic phase does not show up explicitly in an enhanced production of strangeness (or in particular strange mesons and baryons) but leads to a different redistribution of antistrange quarks between mesons and antibaryons. To examine this issue in more detail we show in Fig. 22 the multiplicities of Ξ^- baryons (l.h.s.) and Ξ^+ antibaryons (r.h.s.) - divided by N_{wound} - as a function of the number of wounded nucleons N_{wound} for Pb+Pb collisions at 158 A·GeV at mid-rapidity from PHSD (blue solid lines) and HSD (red dashed-dotted lines) in comparison to the experimental data from the NA57 Collaboration [65] (open triangles) and the NA49 Collaboration [61,62] (solid dots).

The situation is very similar to the case of the strange baryons and antibaryons before: we find no sizeable differences in the double strange baryons from HSD and PHSD - in a good agreement with the NA49 data - but observe a large enhancement in the double strange antibaryons for PHSD relative to HSD. This trend is even more pronounced for triple strange baryons and antibaryons but not shown explicitly here due to the low statistics in the calculations as well as in the experimental data.

Within the HSD and PHSD approaches we may follow explicitly the number of strange and antistrange quarks throughout the reactions. Since the number of $s - \bar{s}$ is zero for all times due to strangeness conservation (and initial vanishing strangeness), we concentrate on the total $s + \bar{s}$ abundancy. Contrary to the early suggestion in Ref. [64] we find that the net $s + \bar{s}$ abundancy is increased only by a few percent during the partonic stage when comparing HSD with PHSD results. Accordingly the number of strange hadrons is also not modified considerably which has been stated some years ago in Ref. [68]. However, the number of antistrange quarks in antibaryons is enhanced by more than a factor two in PHSD relative to HSD (cf. Fig. 23) when considering central collisions of Pb+Pb at top SPS energies.

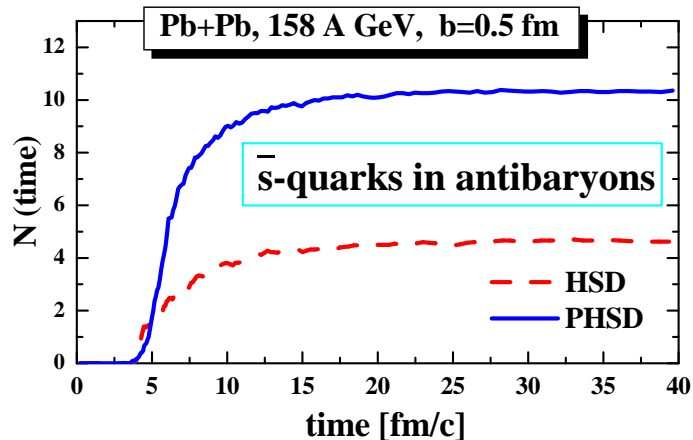


Fig. 23. The number of \bar{s} quarks in antibaryons for central Pb+Pb collisions at 158 A·GeV from PHSD (blue solid line) and HSD (dash-dotted line).

In summarizing this Section we point out that the partonic phase in PHSD leads to a very slight narrowing of the longitudinal momentum distribution of mesons and to a moderate hardening of their transverse mass spectra at SPS energies (close to the data). These effects are not dramatic in the longitudinal degrees of freedom but become clearly visible in the transverse degrees of freedom. The number of $s\bar{s}$ pair production is only slightly enhanced in PHSD relative to HSD, however, the partonic phase in PHSD leads to a significant enhancement in the multistrange antibaryon sector more in line with experimental observations.

4 Summary

In summary, relativistic collisions of Pb+Pb at SPS energies have been studied within the PHSD approach which includes explicit partonic degrees of freedom as well as dynamical local transition rates from partons to hadrons (22), (26). The hadronization process conserves four-momentum and all flavor currents and slightly increases the total entropy since the 'fusion' of rather massive partons dominantly leads to the formation of color neutral strings or resonances that decay microcanonically to lower mass hadrons. Since this dynamical hadronization process slightly increases the total entropy the second law of thermodynamics is not violated (as is the case for simple coalescence models incorporating massless partons).

The PHSD approach has been applied to nucleus-nucleus collisions from 20 to 160 A·GeV in order to explore the space-time regions of 'partonic matter'. We have found that even central collisions at the top SPS energy of ~ 160 A·GeV show a large fraction of non-partonic, i.e. hadronic or string-like matter, which can be viewed as a 'hadronic corona' (cf Refs. [53,54]). This finding implies that neither purely hadronic nor purely partonic 'models' can be employed to extract physical conclusions in comparing model results with data. On the other hand - studying in

detail Pb+Pb reactions at 40, 80 and 158 GeV·GeV in comparison to the data from the NA49 Collaboration - it is found that the partonic phase has only a very low impact on rapidity distributions of hadrons but a sizeable influence on the transverse-mass distribution of final kaons due to the repulsive partonic mean fields and parton interactions.

The most pronounced effect is seen on the production of multi-strange antibaryons due to a slightly enhanced $s\bar{s}$ pair production in the partonic phase from massive time-like gluon decay and a more abundant formation of strange antibaryons in the hadronization process. This enhanced formation of strange antibaryons in central Pb+Pb collisions at SPS energies by hadronization supports the early suggestion of Braun-Munzinger and Stachel [69,70] in the statistical hadronization model - which describes well particle ratios from AGS to RHIC energies. We also mention that partonic production channels for dileptons appear to be visible in the $\mu^+\mu^-$ spectra from In+In collisions at 158 A·GeV in the intermediate invariant mass range [71].

Some note of caution has to be stated here with respect to applications of PHSD at FAIR energies (5-40 A·GeV) since the partonic equation of state employed so far - as fixed to the lQCD results from Ref. [22] - describes a crossover transition between the hadronic and partonic phase while at lower SPS and FAIR energies a first-order phase transition and the appearance of a critical point in the QCD phase diagram are expected [72]. Such phenomena may not be described by the present realization of PHSD but need subtle extensions. On the other hand an application to RHIC energies is rather straight forward - except for a possible color-glass initial state - and detailed results from PHSD will be presented in a separate study.

Acknowledgement

The authors are grateful to O. Linnyk and S. Mattiello for valuable discussions and like to thank H. van Hees for a critical reading of the manuscript. Furthermore, they are indebted to C. Blume, C. Höhne, H. Ströbele, and M. Utvic for providing the data of the NA49 Collaboration in electronic form.

References

- [1] *Quark Matter 2005*, Nucl. Phys. A 774 (2006) 1; *Quark Matter 2006*, J. Phys. G 34 (2007) S1. *Quark Matter 2008*, J. Phys. G 36 (2009) S1.
- [2] E. Shuryak, Prog. Part. Nucl. Phys. 53 (2004) 273.
- [3] M. H. Thoma, J. Phys. G 31 (2005) L7; Nucl. Phys. A 774 (2006) 307.
- [4] A. Peshier and W. Cassing, Phys. Rev. Lett. 94 (2005) 172301.

- [5] I. Arsene *et al.*, Nucl. Phys. A 757 (2005) 1; B. B. Back *et al.*, Nucl. Phys. A 757 (2005) 28; J. Adams *et al.*, Nucl. Phys. A 757 (2005) 102; K. Adcox *et al.*, Nucl. Phys. A 757 (2005) 184.
- [6] T. Hirano and M. Gyulassy, Nucl. Phys. A 769 (2006) 71.
- [7] A. Ayala, M. Martinez, G. Paic, and G. Toledo Sanchez, Phys. Rev. C 77 (2008) 044901.
- [8] S. Scherer *et al.*, New J. Phys. 3 (2001) 8.
- [9] R. C. Hwa and C. B. Yang, Phys. Rev. C 67 (2003) 034902; V. Greco, C. M. Ko and P. Levai, Phys. Rev. Lett. 90 (2003) 202302.
- [10] R. J. Fries, B. Müller, C. Nonaka and S. A. Bass, Phys. Rev. Lett. 90 (2003) 202303.
- [11] Z.-W. Lin *et al.*, Phys. Rev. C 72 (2005) 064901.
- [12] L. Ravagli, H. van Hees and R. Rapp, Phys. Rev. C 79 (2009) 064902; L. Ravagli and R. Rapp, Phys. Lett. B 655 (2007) 126.
- [13] T. S. Biro and K. Urmosy, Eur. Phys. J. ST 155 (2008) 1.
- [14] W. Cassing and E. L. Bratkovskaya, Phys. Rev. C 78 (2008) 034919.
- [15] L. P. Kadanoff, G. Baym, *Quantum Statistical Mechanics*, Benjamin, 1962.
- [16] S. Juchem, W. Cassing and C. Greiner, Phys. Rev. D 69 (2004) 025006; Nucl. Phys. A 743 (2004) 92.
- [17] W. Cassing and S. Juchem, Nucl. Phys. A 665 (2000) 377; *ibid* A 672 (2000) 417.
- [18] Y. B. Ivanov, J. Knoll and D. N. Voskresensky, Nucl. Phys. A 672 (2000) 313; J. Knoll, Y. B. Ivanov, D. N. Voskresensky, Ann. Phys. 293 (2001) 126; Y. B. Ivanov, J. Knoll, and D. N. Voskresensky, Phys. Atom. Nucl. 66 (2003) 1902.
- [19] W. Cassing, E. Phys. J. ST 168 (2009) 3.
- [20] W. Cassing, Nucl. Phys. A 791 (2007) 365.
- [21] W. Cassing, Nucl. Phys. A 795 (2007) 70.
- [22] M. Cheng *et al.*, Phys. Rev. D 77 (2008) 014511.
- [23] A. Nakamura and T. Saito, Phys. Lett. B 621 (2005) 171.
- [24] M. Döring, K. Hubner, O. Kaczmarek, and F. Karsch, Phys. Rev. D 75 (2007) 054504.
- [25] W. Ehehalt and W. Cassing, Nucl. Phys. A 602 (1996) 449.
- [26] W. Cassing and E. L. Bratkovskaya, Phys. Rep. 308 (1999) 65.
- [27] A. Peshier, Phys. Rev. D 70 (2004) 034016; J. Phys. G 31 (2005) S371.
- [28] R. D. Pisarski, Phys. Rev. Lett. 63 (1989) 1129.

- [29] A. Peshier, B. Kämpfer, O.P. Pavlenko, and G. Soff, Phys. Rev. D 54 (1996) 2399; P. Levai and U. Heinz, Phys. Rev. C 57 (1998) 1879; A. Peshier, B. Kämpfer, and G. Soff, Phys. Rev. C 61 (2000) 045203, Phys. Rev. D 66 (2002) 094003.
- [30] M. Bluhm, B. Kämpfer, R. Schulze, D. Seipt, and U. Heinz, Phys. Rev. C 76 (2007) 034901.
- [31] M. Bluhm, B. Kämpfer, R. Schulze, and D. Seipt, arXiv: 0901.0472 [hep-ph].
- [32] J. Letessier and J. Rafelski, Phys. Rev. C 67 (2003) 031902.
- [33] G. Aarts and J. M. Martinez Resco, J. High Energy Phys. 04 (2002) 054; *ibid.* 02 (2004) 030.
- [34] B. D. Serot and J. D. Walecka, Adv. Nucl. Phys. 16 (1988) 1.
- [35] T. Maruyama, W. Cassing, U. Mosel, S. Teis, K. Weber, Nucl. Phys. A 573 (1994) 653.
- [36] C. B. Dover, U. Heinz, E. Schnedermann, and J. Zimanyi, Phys. Rev. C 44 (1991) 1636.
- [37] S. J. Wang *et al.*, Nucl. Phys. A 573 (1994) 245.
- [38] W. Cassing, E. L. Bratkovskaya and X.-Y. Xing, Prog. Part. Nucl. Phys. 62 (2009) 359.
- [39] H.-U. Bengtsson and T. Sjöstrand, Comp. Phys. Commun. 46 (1987) 43.
- [40] T. Falter, W. Cassing, K. Gallmeister, and U. Mosel, Phys. Rev. C 70 (2004) 054609.
- [41] E. L. Bratkovskaya and W. Cassing, Nucl. Phys A 807 (2008) 214.
- [42] A. Lang, H. Babovsky, W. Cassing, U. Mosel, H.-G. Reusch, and K. Weber, J. of Comp. Phys. 106 (1993) 391.
- [43] W. Cassing, Nucl. Phys. A 700 (2002) 618.
- [44] Z. Xu and C. Greiner, Phys. Rev. C 71 (2005) 064901, Nucl. Phys. A 774 (2006) 034909; Phys. Rev. C 79 (2009) 014904.
- [45] T. Sjöstrand *et al.*, Comp. Phys. Commun. 135 (2001) 238.
- [46] H. Petersen, J. Steinheimer, G. Burau, M. Bleicher and H. Stöcker, Phys. Rev. C 78 (2008) 044901.
- [47] H. Petersen, J. Steinheimer, G. Burau and M. Bleicher, Eur. Phys. J. C 62 (2009) 30.
- [48] H. Petersen and M. Bleicher, Phys. Rev. C 79 (2009) 054904.
- [49] S.A. Bass, M. Belkacem, M. Bleicher, M. Brandstetter, L. Bravina, C. Ernst, L. Gerland, M. Hofmann, S. Hofmann, J. Konopka, G. Mao, L. Neise, S. Soff, C. Spieles, H. Weber, L.A. Winkelmann, H. Stöcker, W. Greiner, Ch. Hartnack, J. Aichelin, and N. Amelin, Prog. Part. Nucl. Phys. 42 (1998) 279.

- [50] M. Bleicher, E. Zabrodin, C. Spieles, S.A. Bass, C. Ernst, S. Soff, L. Bravina, M. Belkacem, H. Weber, H. Stöcker, and W. Greiner, *J. Phys. G* 25 (1999) 1859.
- [51] L. McLerran, *Nucl. Phys. A* 787 (2007) 1; *Int. J. Mod. Phys. A* 21 (2006) 694.
- [52] W. Cassing and C. M. Ko, *Phys. Lett. B* 396 (1997) 39.
- [53] J. Aichelin and K. Werner, arXiv:0810.4465 [nucl-th]; K. Werner, *Phys. Rev. Lett.* 98 (2007) 152301.
- [54] F. Beccattini and J. Manninen, *J. Phys. G* 35 (2008) 104013.
- [55] C. Blume et al., NA49 Collaboration, *J. Phys. G: Nucl. Part. Phys.* 35 (2008) 044004.
- [56] H. Ströbele et al., NA49 Collaboration, Proceedings of the CPOD-2009: Workshop on 'Critical Point and Onset of Deconfinement', Brookhaven, June 8-12 (2009).
- [57] C. Alt et al., NA49 Collaboration, *Phys. Rev. C* 66 (2002) 054902; *Phys. Rev. C* 77 (2008) 024903.
- [58] E. L. Bratkovskaya, S. Soff, H. Stöcker, M. van Leeuwen, and W. Cassing, *Phys. Rev. Lett.* 92 (2004) 032302.
- [59] E. L. Bratkovskaya, W. Cassing, and H. Stöcker, *Phys. Rev. C* 67 (2003) 054905.
- [60] E. L. Bratkovskaya *et al.*, *Phys. Rev. C* 69 (2004) 054907.
- [61] C. Alt et al., NA49 Collaboration, *Phys. Rev. C* 78 (2008) 034918.
- [62] T. Anticic et al., NA49 Collaboration, arXiv:0906.0469 [nucl-ex].
- [63] J. Geiss, W. Cassing and C. Greiner, *Nucl. Phys. A* 644 (1998) 107.
- [64] J. Rafelski and B. Müller, *Phys. Rev. Lett.* 48 (1982) 1066.
- [65] F. Antinori *et al.*, *Phys. Lett. B* 595 (2004) 68; *J. Phys. G: Nucl. Phys.* 32 (2006) 427.
- [66] C.H. Li and C.M. Ko, *Nucl. Phys. A* 712 (2002) 110.
- [67] L.W. Chen, C.M. Ko, and Y. Tzeng, *Phys. Lett. B* 584 (2004) 269.
- [68] H. Weber, E. L. Bratkovskaya, W. Cassing, and H. Stöcker, *Phys. Rev. C* 67 (2003) 014904.
- [69] P. Braun-Munzinger *et al.*, *Phys. Lett. B* 365 (1996) 1; *ibid.* B 465 (1999) 15; *ibid.* B 518 (2001) 41.
- [70] A. Andronic, P. Braun-Munzinger and J. Stachel, *Nucl. Phys. A* 772 (2006) 167.
- [71] O. Linnyk, E. L. Bratkovskaya, and W. Cassing, arXiv: 0907.4255 [nucl-th].
- [72] P. Senger *et al.*, CBM Physics Book, Springer, in press.